ELSEVIER

# Simulating gear and bearing interactions in the presence of faults Part I. The combined gear bearing dynamic model and the simulation of localised bearing faults

N. Sawalhi*, R.B. Randall[1]

*School of Mechanical and Manufacturing Engineering, The University of New South Wales, Sydney 2052, Australia*

## Abstract

This paper presents a simulation model for a gearbox test rig, in which a range of bearing faults can be implemented. Bearing faults sometimes manifest themselves by their interaction with meshing gears, and to simulate this it is necessary to model a whole system of gears and shafts supported in bearings. This has now been done for an experimental test rig through the incorporation of a time-varying, non-linear stiffness bearing model into a previously developed gear model. The incorporated bearing model is based on Hertzian contact theory, which relates the raceway displacement to the bearing load, and also accounts for the slippage between the elements. It has the capacity to model localised spalls (inner race, outer race and rolling elements), which are discussed in this part of the paper and extended inner and outer race faults (rough surfaces), which are discussed in part II. Even though the whole gearbox has not been modelled in detail, the non-linear time-varying gear-meshing operation is modelled in some detail. Both simulated and experimental localised fault signals (acceleration signals) were subjected to the same diagnostic techniques; namely spectrum comparisons, Spectral Kurtosis (SK) analysis and envelope analysis. The processed simulated signals showed a similar pattern to that observed in their measured counterparts and were found to have a characteristic, referred to in the literature as double pulses, corresponding to entry into and exit from the localised fault. The simulation model will be useful for producing typical fault signals from gearboxes to test new diagnostic algorithms, and possibly prognostic algorithms.
© 2007 Elsevier Ltd. All rights reserved.

*Keywords:* Rolling element bearings; Gears; Localised fault; Spall; Spectral Kurtosis (SK); Envelope analysis; Gear/bearing interaction; Time-varying systems; Hertzian contact

## 1. Introduction

In order to facilitate the development of diagnostic and prognostic techniques for rolling element bearings in real systems, a necessity existed for producing simulation models, where faults can be implemented under

*Corresponding author. Tel.: +61 2 9385 5676.
  *E-mail addresses:* n.sawalhi@unsw.edu.au (N. Sawalhi), b.randall@unsw.edu.au (R.B. Randall).
[1]Tel.: +61 2 9385 5697.

different operating conditions rather than waiting for these to occur naturally, or alternatively having them seeded in the laboratory.

Such fault simulation can be very valuable in machine diagnostics and prognostics in order to produce signals with well-defined characteristics. For example, the signals could be used to train neural networks to perform diagnostics and prognostics of a range of different fault types and locations in machines. These usually require so much data to train them that it would not be economical to actually experience the number of faults of each type required to accomplish the training.

This paper presents a simulation model for a gearbox test rig, in which a range of bearing faults can be implemented. The gearbox test rig model described in Ref. [1] is presented in Section 2. This was updated by using a bearing model (two-dimensional model) similar to that in Ref. [2], with the capability of introducing geometrical faults (localised spalls). Section 3 discusses the bearing model, which includes the slippage, the inner/outer race localised fault modelling and the modelling of localised faults in rolling elements. Note that in the bearing model, the gearbox casing was included (not discussed in previous models) so that the vibration response, even at high frequencies, could be extracted for comparison with that done experimentally. Noise was added to the obtained response signals so that a reasonable signal-to-noise ratio (SNR) is achieved (15–25 dB). This noise represents the random part of the excitation, which includes all the disturbances (load variations, bearing friction, etc.). Section 4 discusses the dynamics of the gears, while Section 5 presents the combined gear-bearing model building on the presentation of Sections 2–4. The comparison between the simulated results and the experimental results is presented in Section 6 for the three types of localised faults in the bearing, viz. inner/outer races and rolling elements.

While this part of the paper (part I) is concerned with the modelling of localised faults, the second part (part II) discusses the modelling of extended faults and compares the simulated results with those experimentally obtained for extended inner and outer race faults.

Some of the theoretical development of this paper was presented in conference papers [3,4].

## 2. The spur gear test rig and its initial simulation models

The gearbox test rig (Fig. 1) under investigation was built by Sweeney [5] to investigate the effect of gear profile errors on transmission error (TE). In this test rig, the single stage gearbox (in this case a spur gear set with 1:1 ratio and 32 teeth on each gear) is driven primarily by a three-phase electric motor, but with circulating power via a hydraulic pump/motor set. The input and output shafts of the gearbox are arranged in parallel and each shaft is supported by two double row ball bearings (Koyo 1205). The flywheels are used to reduce the fluctuations of the input and output shaft speeds. The couplings are flexible in torsion and without stiffness in bending, making them very helpful for the attenuation of the shaft torsional vibration.

Different mathematical models have been developed to study the dynamic effects on the TE of the gearbox. These were lumped parameter models (LPM), which assume that each shaft mass and inertia is lumped at the bearings or at the gears. Sweeney [5] modelled the rig using six degrees of freedom (DOF), all of which were torsional vibrations. In his model, the tooth pair meshing stiffness was simplified as a constant (although the number of pairs in mesh at a given roll angle varied according to the contact ratio). A more complex model was developed by Du [6], who retained the original DOF and added six more to account for the bending and lateral motions.

Gao and Randall [7] developed a 16-DOF model. They excluded the two-DOF at the motor and the pump (as their effect is isolated by the two flywheels) and instead included the two encoders due to the relevance of their torsional resonance.

Finally Endo [1] and Endo et al. [8] employed the 16-DOF model to simulate spalls and cracks in gear teeth and to develop diagnostic techniques to differentiate between the two. This was done using a finite element programme to simulate the variation of the mesh stiffness for the two types of faults under varying static load conditions, which was then used (as a lookup table with interpolation) in the lumped parameter dynamic model of the simulated gearbox to obtain the dynamic TE and the acceleration responses under different loads and speeds.

In all the previously discussed models, rolling element bearings (REBs) were modelled as a single-DOF (mass-spring) system with constant stiffness.
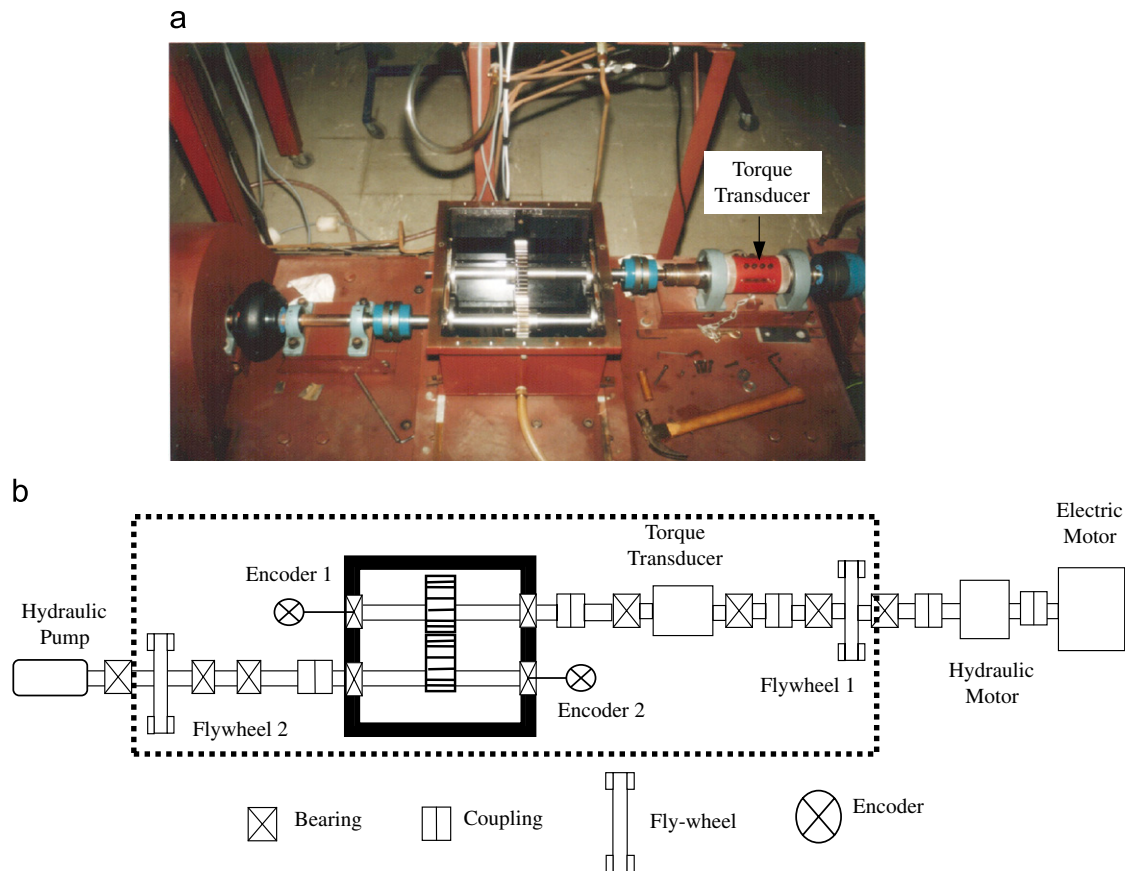
a



b



Fig. 1. University Of New South Wales (UNSW) spur gear test rig: test rig photo (a), schematic diagram (b).

## 3. Rolling element bearing modelling

### 3.1. A review of the dynamic modelling of rolling element bearings

The first few major works on rolling element bearing dynamic modelling were performed by Lundberg and Palmgren [9] and Harris [10], who described both radial and axial load deflections using non-linear stiffness coefficients, but did not conventionally address the total non-linearity and time-varying characteristics of the rolling element bearings. The first attempt to complete a dynamic model of rolling element bearings was reported by Gupta [11] through solving the generalised differential equations of motion of the ball in an angular contact ball bearing. For a review on the different bearing dynamic models, especially the ones discussed by Gupta, see Ref. [12].

Time-variant characteristics in rolling element bearings are a direct result of the orbital motion of the rolling elements (time-invariant models assume fixed element positions). Rolling element bearings generate vibrations even when the geometry of the bearing elements is ideal. Varying compliance vibration is caused by the varying orbital position of the balls. This movement leads to fluctuations in the stiffness of the bearing [13].

Non-linearity in rolling element bearings arises from non-linearity effects due to the Hertzian force/ deformation relationship, the varying stiffness resulting from load transmission via a finite number of rolling elements, the presence of clearance between the rolling elements and the bearing races, and the effect of the lubricant film.

Tiwari et al. [14,15] studied the effect of the ball bearing clearance on the dynamic response of a rigid rotor. The effect of unbalance of the rigid rotor was also included in their simulation model [15]. Tiwari et al.

noticed that the stiffness of the bearing increases as the clearance decreases. They also reported that the non-linearity of the ball bearing–rotor system increases when the bearing clearance increases.

Elasto-hydrodynamic lubrication (EHL) was introduced into the modelling in the mid-1960s. Wijnat et al. (1999) [16] reviewed the studies concerning the effect of the EHL on the dynamics of the rolling element bearings and developed computational models for both the EHL problem and the structural dynamics problem to study the influence of the EHL on the bearing dynamics. The interaction between the structural elements was described by means of a non-linear spring-damper model, which was based on numerical solutions of the full EHL contact problem. This effect of the EHL, as compared to the dry contact situation was found to be moderate for medium loads and low rotational speeds and showed an increase for low loads and higher speeds.

One of the most comprehensive models, which address the non-linearity and the time-variant characteristic of rolling element bearings (but not the EHL effect), was presented by Fukata et al. [17]. The dynamic model of Fukata is a two-DOF model, which is based on the Hertzian theory that relates the raceway displacement vector to the bearing load vector (see Section 3.2). This work has since been further developed by Feng et al. [2] by including the effect of slippage of the cage and rolling elements, and also by including the effect of localised faults (spalls) in the inner and outer races (see Section 3.3). The models also include the clearance of the bearing and the possibility of studying the effect of any unbalance. The details of the bearing simulation models of Fukata and Feng are discussed fully as they have been adopted here to form the basis for a complete gear-bearing model.

One of the new comprehensive models found in literature for the dynamics of rolling element bearings is Sopanen and Mikkola's model [13,18], which included the effect of different geometrical faults (surface roughness, waviness and localised and distributed effects) and the EHL. The dynamic model of the deep-groove ball bearing is a six-DOF model, which included both the non-linear Hertzian contact deformation and the elasto-hydrodynamic fluid film. The geometry, material properties and diametral clearance of the bearing were given as the input to the model. The bearing force and torque components were calculated from the relative displacements and velocities between bearing rings. Distributed defects, such as the waviness of the inner and outer ring, and localised defects, such as inner and outer ring defects, were taken into consideration in the model. The model of the ball bearing was implemented and analysed using a commercial multi-body system software application (MSC.ADAMS). The simulation results were compared with analytical results and with reported measurements taken from literature. The results demonstrated that the analytical results agreed well with the results of the simulation. It was observed that the diametral clearance has a significant effect on the natural frequencies and the vibration response of the system. Ball bearings with an ideal geometry generate vibration owing to the varying compliance effect. Un-balance excitation and the varying compliance effect generate sum and difference frequencies. The low-order waviness (out-of-roundness) of the rotating bearing ring produces excitations at frequencies equivalent to the rotation speed times the order of waviness. Localised defects also generate vibrations at the bearing defect frequencies. The spectra obtained by the proposed model are in accordance with reported experimental spectra.

Sopanen and Mikkola's paper [13] also contains a useful review of the different dynamic models, which discuss the effect of waviness, EHL, localised defects and the clearance effects. The relevance of this to our models is discussed in Section 3.4.

Some dynamic models are readily available for general use, an example of which is ADORE (Advanced Dynamics of Rolling Elements) [19] and BEAST (BEAring Simulation Tool). The program BEAST is developed by SKF® and PELAB® to perform simulations of bearing dynamics on any major bearing type. BEAST is a fully three-dimensional program used to perform simulations of bearing dynamics on any major bearing type which enables studies of internal motions and forces in a bearing under any given loading condition.

As the dynamic modelling of the rolling element bearings has been extensively developed, different studies are emerging to combine the bearing model with other rotating parts in the machine (rotors, gears, etc.) in order to study the effect of the vibration induced by bearings on other components. For instance, Lim and Singh [20,21] studied the vibration transmitted through rolling element bearings in rotor systems and in geared rotors.

### 3.2. Rolling element bearing model (fault free case with no slippage)

The main fundamental components of a rolling element bearing are the outer race, the inner race, the cage and the rolling elements. The important geometrical quantities are the number of rolling elements $n_b$, the element diameter $D_b$, the pitch diameter $D_p$ and the contact angle $\alpha$. Fig. 2a shows these parameters and components along with the load zone associated with a unidirectional vertical load.

The model discussed ahead was originally developed by Fukata et al. [17]. It provides the basis for the following developments. The non-linearity in a rolling bearing, arising from the non-linear forces between the different elements (Hertzian contact), the time-varying stiffness (load transmission dependency on the positioning of the supporting elements) and the clearance between the rolling elements and the bearing races, have been incorporated into this model. This gives a much-improved simulation of the dynamics of the REBs.

The bearing was modelled as a two-DOF system, which provides the load–deflection relationships, while ignoring the mass and the inertia of the rolling elements. The two orthogonal DOF are related to the inner race (rotor). Contact forces are summed over each of the rolling elements to give the overall forces on the shaft in the load direction and at right angles to it. Fig. 2b explains the essentials of this model as presented by Liew et al. [22], who gave an interesting summary presentation of four different ways to model the bearing, and used them in a transient software (developed in FORTRAN) to study the dynamics of a rotor system. All these models (two DOF with and without inertia and five DOF with and without inertia) are based upon the Hertzian contact relationship [10].

The overall contact deformation (contact compression) for the $j$th rolling element $\delta_j$ is a function of the inner race displacement relative to the outer race in the $x$- and $y$-directions ($x_s$, $y_s$), the element position $\phi_j$ (time varying) and the clearance ($c$). This is given by

$$\delta_j = x_s \cos \phi_j + y_s \sin \phi_j - c \quad j = 1, 2, \ldots, n_b. \tag{1}$$

Accounting for the fact that compression occurs only for positive values of $\delta_j$, $\gamma_j$ (contact state of $\delta_j$ the rolling elements) is introduced as

$$\gamma_j = \begin{cases} 1 & \text{if } \delta_j > 0 \\ 0 & \text{otherwise.} \end{cases} \tag{2}$$

The angular positions of the rolling elements $\phi_j$ are functions of time increment $dt$, the previous cage position $\phi_o$ and the cage speed $\omega_c$ (can be calculated from geometry and the shaft speed $\omega_s$ assuming no slippage) are given as

$$\phi_j = \frac{2\pi(j-1)}{n_b} + \omega_c dt + \phi_o \tag{3}$$

$$\omega_c = \left(1 - \frac{D_b}{D_p}\right) \frac{\omega_s}{2}. \tag{4}$$

The ball raceway contact force $f$ is calculated using traditional Hertzian theory (non-linear stiffness) from
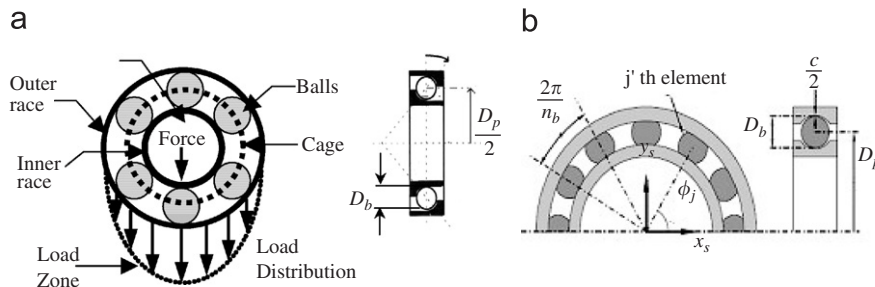
$$f = k_b \delta^n. \tag{5}$$



Fig. 2. (a) Rolling element bearing components and load distribution, (b) two degree-of-freedom model [10].

The load deflection factor $k_b$ depends on the contact geometry and the elastic contacts of the material, and exponent $n = 1.5$ for ball bearings and 1.1 for roller bearings. Using Eq. (5) and summing the contact forces in the x- and y-directions for a ball bearing with $n_b$ balls, the total force can be calculated as follows:

$$f_x = k_b \sum_{j=1}^{n_b} \gamma_j \delta_j^{1.5} \cos \phi_j, \tag{6}$$

$$f_y = k_b \sum_{j=1}^{n_b} \gamma_j \delta_j^{1.5} \sin \phi_j. \tag{7}$$

The stiffness of the bearing as presented by this model is non-linear, and is time varying in nature as the positions of the rolling elements (function of time) determine the overall contact.

### 3.3. Bearing-pedestal model with slippage and localised faults in the inner or outer races

Building on the bearing model of Fukata et al. [17], Feng et al. [2] developed a bearing-pedestal model. The DOF for this model are four, as it includes the pedestal (two DOF). It takes into consideration the slippage in the rolling elements (uncertainty in ball positions), the effect of mass unbalance in the rotor and the possibility of introducing a localised fault (spall) in the inner or outer races. Slippage in bearings occurs as a result of the variation of the load angle for each rolling element, since the kinematic bearing characteristic frequencies contain a general $\cos \alpha$ term. The random fluctuation of the ball positions as a result of this can be either forward or backward of the mean. This was related to the nominal motion of the cage ($\omega_c dt$) and was modelled by introducing random numbers of zero average with uniformly distributed fluctuations within $\phi_{j,\,rand} = \pm 1.5 \omega_c dt \ (\pm 0.05°)$.

### 3.4. The new bearing-pedestal model

The model of Feng et al. [2] has been adopted here for studying the dynamics of rolling element bearings and has now an extra DOF (small sprung mass with relatively high damping to represent a typical high frequency). The new model has five DOF and is symbolically represented in Fig. 3.

Although the effects of EHL were not added to the model when adopting it here—due to excessive computational demands in the analysis—the effects of the EHL are somewhat integrated in the model. The EHL stiffness modelling generally increases the stiffness of the bearing over the purely Hertzian analysis as the



$x_s, y_s$: Shaft/inner race DOF
$x_p, y_p$: pedestal/outer race DOF
$y_b$: Measured vibration response
$k_p$: pedestal stiffness
$k_s$: shaft Stiffness
$k_r$: Stiffness of sprung system
$c_p$: Damping in pedestal
$c_r$: Damping in sprung system
$m_s$: Mass of shaft/inner race
$m_p$: Mass of pedestal
$m_r$: Mass of resonance changer
$\omega_s$: Shaft rotational speed
$f_{b8}$: Ball race way contact force for element 8

Spring mass system to simulate a typical high frequency resonant response of the bearing (stiffness and damping selected to excite a 15 kHz frequency with 5 % damping)
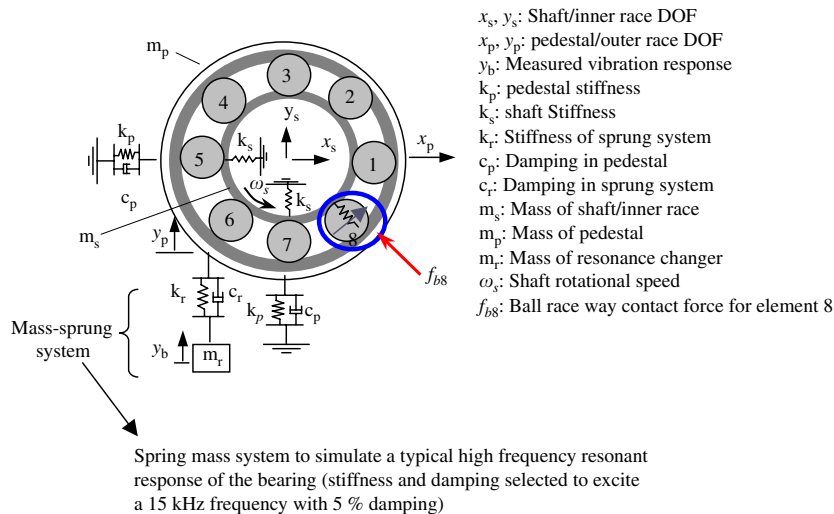
Fig. 3. Five-DOF bearing-pedestal model.

EHL film takes up some of the clearance of the bearing and can even create negative clearance or preload (Wijnat et al., 1999) [16]. This effect can be obtained in the current model by setting the clearance value ($c$) in Eq. (1) to a negative value. The bearing damping, which is determined using EHL theory, has also been taken into the consideration by considering a viscous damping (constant percentage ranging from 2% to 5%) in the model.

The gear test rig modelled runs at a maximum speed of 14 Hz (840 rpm) which is very low. Results were obtained at speeds up to 10 Hz (600 rpm). Liew et al. found that the effect of rolling element inertia is minimal on the two-DOF model and that the effect of rolling element inertia is only significant and needs to be considered only at higher speeds (Liew et al. [22] tested different models in the speed ranges of 5000–18,000 rpm).

The general equations of motion for this rotor-bearing system, taking into consideration the non-linear contact stiffness can be expressed by Eqs. (8–12).

$$m_s \ddot{x}_s + k_s(x_s) + (f_x((x_s - x_p), \omega_s, \mathrm{d}t) = 0, \tag{8}$$

$$m_s \ddot{y}_s + k_s(y_s) + f_y((y_s - y_p), \omega_s, \mathrm{d}t) = 0, \tag{9}$$

$$m_p \ddot{x}_p + c_p \dot{x}_p + k_p x_p - f_x((x_s - x_p), \omega_s, \mathrm{d}t) = 0, \tag{10}$$

$$m_p \ddot{y}_p + (c_p + c_r)\dot{y}_p + (k_p + k_r)y_p - k_r y_b - c_r \dot{y}_b - f_y((y_s - y_p), \omega_s, \mathrm{d}t) = 0, \tag{11}$$

$$m_r \ddot{y}_b + k_r(y_b - y_p) + + c_r(\dot{y}_b - \dot{y}_p) = 0. \tag{12}$$

There are five DOF in the new model in contrast to the model of Fukata et al. [17], as it introduces two extra DOF for the pedestal ($x_p$, $y_p$) and another DOF to measure the high frequency bearing response ($y_b$).

For the new model, on the one hand, the mass and the stiffness of the pedestal were adjusted to match a low natural frequency of the system (obtained by a modal test) [1]. On the other hand, the stiffness and the damping of the additional spring-mass system were selected so that a typical high frequency resonant response of the bearing is excited (15 kHz with 5% damping).

Note that Eq. (5) will still hold for calculating the contact forces in the bearing ($f_x$, $f_y$); however, the overall deflection $\delta_j$ previously calculated using Eq. (1) has three main variations to reflect: (a) the modelling of the pedestal, (b) the possibility of a localised fault in one of the races and (c) the slippage in the rolling elements, which is incorporated in the ball position ($\phi_j$) and is presented in Eq. (13).

Eq. (1), including these new variations, can be rewritten as follows:

$$\delta_j = (x_s - x_p)\cos \phi_j + (y_s - y_p)\sin \phi_j - c - \beta_j C_d. \tag{13}$$

### 3.4.1. Slippage

The angular position of the ball $j$ including the slippage is expressed as follows:

$$\phi_j = \frac{2\pi(j - 1)}{n_b} + \omega_c \mathrm{d}t + \overbrace{\phi_o}^{\text{preivous cage position}} + \overbrace{(0.5 - rand) \times \phi_{slip}}^{\text{slippage}}. \tag{14}$$

The slippage as defined by Eq. (14) is based on the phase deviation $\phi_{slip}$. The relation between the frequency deviation and the phase deviation is given in Eq. (15) (Randall, 1987 [23]).

$$\Delta f = \phi_{slip} f_m, \tag{15}$$

where $\Delta f$ is the maximum frequency deviation (Hz), $f_m$ is the modulation frequency (Hz) and $\phi_{slip}$ is the maximum phase deviation (rad).

In rolling element bearings, the slippage is defined in terms of a percentage variation of the mean frequency of impact ($\Delta f/f_m \times 100\%$), and is usually between 1% and 2%. This corresponds to a phase variation ($\phi_{slip}$) of (0.01–0.02 rad).

### 3.4.2. Inner/outer race localised fault modelling

A spall of a depth ($C_d$) over an angular distance of ($\Delta\phi_d$) is modelled using the fault switch $\beta_j$ to simulate the contact loss at a defined angular position ($\phi_d$). This in turn defines the spall region as a step function—as shown in Fig. 4 and further illustrated by Fig. 5a—in which $\beta_j$ is defined as follows:

$$\beta_j = \begin{cases} 1 & \text{if } \phi_d < \phi_j < \phi_d + \Delta\phi_d, \\ 0 & \text{otherwise.} \end{cases} \tag{16}$$

The outer race spall is fixed in location between $\phi_d$ and $\phi_d + \Delta\phi_d$. This normally occurs in the load zone. An inner race spall rotates at the same speed as the rotor, i.e. $\phi_d = \omega_s t + \phi_{do}$ ($\phi_{do}$, initial starting location of the spall). Note that the spall on the inner race is associated with the speed of the shaft.

The modelling of the spall as presented in Ref. [2] assumes that the rolling element will lose contact suddenly once it enters the spall region, and will regain contact instantly when exiting from that area. This way of modelling results in very large impulsive forces in the system as a consequence of the acceleration increasing sharply in order to maintain balance within the system.

In order to model the behaviour of the rolling element to reflect the actual path the rolling element takes while rolling into and out of the spall region (closer to reality), the depth of the defect $C_d$ should be redefined as a function of $\phi$ so that a gradual rather than instant loss/gain of contact is achieved. The new definition of the depth of defect compared to the one presented above is illustrated in Fig. 5b (not to scale, showing the switch status between the two models).

### 3.5. Modelling localised faults in rolling elements

For a complete modelling of localised faults, the new model was updated to enable simulating faults in the rolling elements. A spall on one of the rolling elements (rolling element $k$) rotates at the same speed as the rolling element, i.e. $\omega_{\text{spin}}$ (ball spin frequency), which is defined in Eq. (17) as

$$\omega_{spin} = \frac{\omega_s}{2} \frac{D_p}{D_b} \left( 1 - \left( \frac{D_b}{D_p} \cos \alpha \right)^2 \right). \tag{17}$$
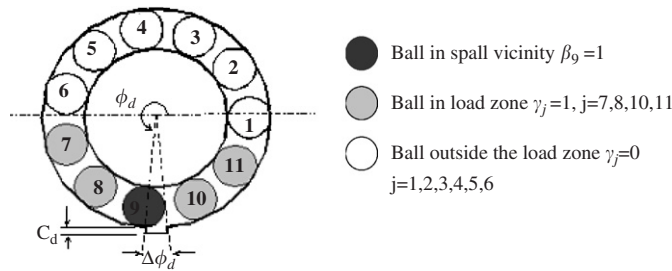


Fig. 4. Spall definition on the outer race.



Fig. 5. Spall definition update: (a) original (b) updated.

The position of the spall ($\phi_s$) can be defined as in Eq. (18)

$$\phi_s = \omega_{spin}t + \phi_{do},$$
(18)

where $\phi_{do}$ is the initial starting location of the spall.

The position of the spall is associated with the speed of the rolling element, which in turn is a function of the shaft speed. This means that the rolling element faults share some characteristics with faults on the inner race and define a main difference from the faults associated with the outer race (fixed location).

The loss of contact is detected for only the faulty rolling element $k$, and this is done twice for each complete rotation of that rolling element, i.e. when it is in touch with the inner race and with the outer race.

Note that the switch values and the periods of switching on ($\Delta\phi_d$) will not be the same for both races, which results from the difference in curvature between the two races and this is also a function of the rolling element diameter. The inner race will contact deeper and longer compared to the outer race. Instead of defining two spall geometries, the fault $\beta_j$ switch can be modified to show this variation as sensed by the different races as in Eq. (19).

$$\beta_j = \begin{cases} 0 & j \neq k, \\ \left. \begin{array}{ll} 1 & \text{if } 0 < \phi_s < \Delta\phi_{do} \\ \frac{C_{dr}+Cd_i}{C_{dr}-Cd_o} & \text{if } pi < \phi_s < (pi + \Delta\phi_{di}) \end{array} \right\} & j = k, \\ 0 & \text{otherwise.} \end{cases}$$
(19)

The derivation of the switch values is illustrated in Fig. 6 (not to scale), when the spalled rolling element is in touch with the inner race. For this case, the total loss of contact, as a result of creating a slot of width $2x$, is the summation of two values. The first is the maximum depth the inner race will enter in the slot region ($C_{di}$ as calculated in Eq. (20), which represents the movement of the inner race from its original contact position—moving downwards). The second represents the movement of the ball from its original contact position as a result of creating the slot ($C_{dr}$ as presented in Eq. (21)—moving upwards).

Note that when the spalled element is in touch with the outer race, the net change in the contact ($C_d$) is the difference between the rolling element movement ($C_{dr}$) and outer race movement ($C_{do}$) as shown in Eqs. (22) and (23), respectively. This is due to the fact that the outer race moves downwards and so does the rolling element, which means that the net change in the contact between the original and the new contact position can be obtained by subtracting the two changes.

$$C_{di} = r_i - \sqrt{r_i^2 - x^2} \quad \text{(maximum depth the inner race will reach)},$$
(20)



$$r_i = \frac{D_p - D_b}{2} \quad \text{(Inner race radius)}$$

$$x = \Delta\phi_d \frac{D_b}{4} \quad \text{(Half the spall width)}$$
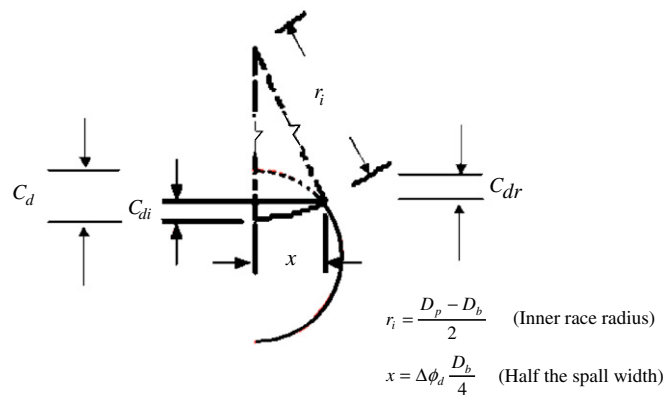
Fig. 6. Rolling element spall depth as sensed by the inner race (not to scale).

$$C\,dr = \frac{D_b}{2} - \sqrt{\left(\frac{D_b}{2}\right)^2 - x^2} \quad \text{(maximum contact loss in the rolling element contact as a}$$

result of the spall). $\hspace{11cm}$ (21)

Similarly,

$$ro = \frac{D_p + D_b}{2} \quad \text{(outer race radius).} \hspace{6cm} (22)$$

$$C_{do} = ro - \sqrt{r_o^2 - x^2} \quad \text{(maximum depth the outer race will reach).} \hspace{3cm} (23)$$

The angular widths of the fault will also depend on the race contacting the defective roller and are given by Eqs. (24) and (25) for outer and inner race contact, respectively.

$$\Delta\phi_{d_o}(\text{rad}) = \frac{2x}{ro} \quad \text{(angular width of the fault as sensed by the outer race),} \hspace{2cm} (24)$$

$$\Delta\phi_{d_i}(\text{rad}) = \frac{2x}{ri} \quad \text{(angular width of the fault as sensed by the inner race).} \hspace{2cm} (25)$$

## 4. Gear dynamics (based on Ref. [1])

Using a lumped parameter model, a pair of meshing gears can be modelled as a pair of cylindrical masses (Fig. 7) connected by a position-dependant stiffness variable $k_m(\theta)$, a damping coefficient $c_m$ and a combined effect of tooth topography deviations and misalignment of the gear pair $e_t(\theta)$ [1].

In this model [1], the $e_t(\theta)$, i.e. the effect of Geometric Transmission Error (GTE) was estimated based on combined waveform expressions of the run-out and the toothprofile errors as follows:

$$e_t(\theta) = e_{runout} + e_{toothprofile}, \hspace{7cm} (26)$$

runout error ($e_{runout}$),



θ_pin, θ_ge: Angular position of the pinion, gear
J_pin, J_ge: Mass moment of inertia of pinion and gear
x_pin, y_pin, x_ge, y_ge: Translational degrees of freedom for the pinion and gear
m_pin, m_ge: Mass of pinion and gear
k_s (1,2): Stiffness of pinion/gear shaft and support
c_m, Damping in gear mesh k_m (θ) : Gear mesh stiffness
e_t (θ): Displacement due to gears' profile error
r_pin, r_ge: Radii of pinion and gear
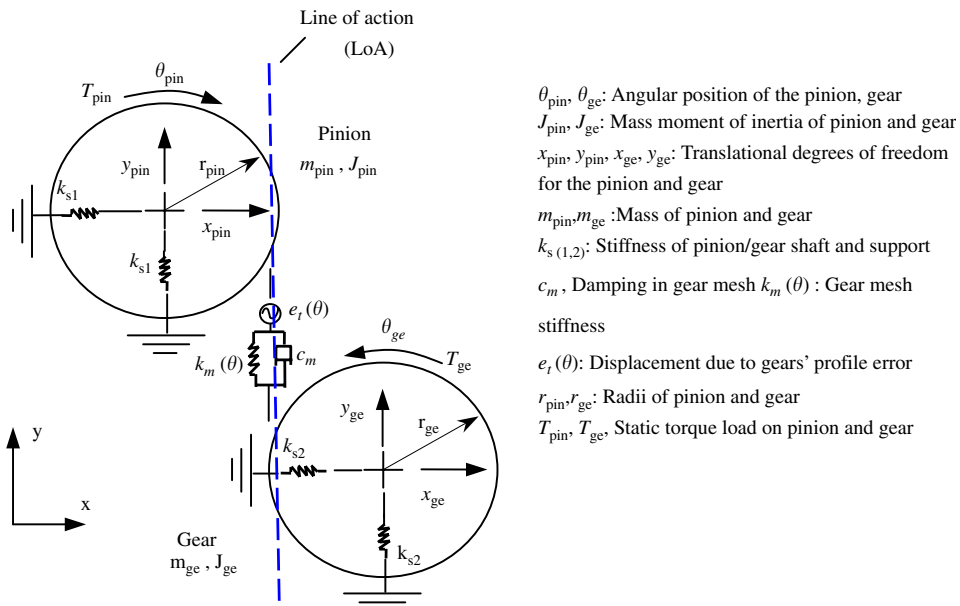T_pin, T_ge, Static torque load on pinion and gear

Fig. 7. Lumped parameter model for the pinion and the gear.

$$e_{runout} = 30 \times 10^{-6} \sin\left(\frac{2\pi t}{T} + \varphi_k\right), \tag{27}$$

toothprofile error ($e_{toothprofile}$),

$$e_{toothprofile} = 12 \times 10^{-6} \sin\left(\frac{2\pi tN}{T} + \varphi_k\right), \tag{28}$$

where $N$ is the number of teeth on a gear, $T$ is the shaft rotational period and $\varphi_k$ is the phase difference.

As only the low harmonic components of the TE (as modelled in Ref. [1]) have been considered above and the TE components are generated separately without taking into consideration the effect of torque variation, an error term (broadband noise) has been added to the TE components. As this noise is introduced to the system as an input, it will act to produce multiplicative noise which evidently has a narrow band filtering effect. This greatly improves the similarities between the simulated and actual measured signals (see Fig. 13). The new definition of the GTE, which includes the effect of noise, is shown in Eq. (29).

$$e_t(\theta) = e_{runout} + e_{toothprofile} + \overbrace{0.2 \times 10^{-6} \, randn}^{\text{error term}}. \tag{29}$$

The $k_m(\theta)$ was obtained by using static simulation. In the static simulation, the load dependant non-linearity of gearmesh stiffness, caused by the effect of Hertzian contact between the meshing gear teeth, was considered by means of tabulated values of time-varying gearmesh stiffness over a range of loads, with cubic spline interpolation. The use of the gearmesh stiffness computed from the static model can be justified as long as the behaviour of the meshing teeth can be described by their stiffness properties only. The inertia of the gear teeth would only be significant at much higher frequencies [1]. The obtained $e_t(\theta)$ and $k_m(\theta)$ values were then directly introduced to the dynamic model as a "look-up table" format.

Forces in the direction normal to the Line of Action (LoA) (e.g. the effect of the friction) are not included in this model. The results of simulation conducted by Howard et al. (2001) [24] shows that the friction has a very small effect on the vibration waveforms of the operating gears. Note that all mesh damping has been assigned to the normal DOF even though some may be due to the sliding friction [1].

The gearmesh was assumed free from contact loss due to the assumption (tested in practice) that the gears operate under sufficient load [1].

The DOF contained in this model are two rotational ($\theta_{pin}$, $\theta_{ge}$) and four translational ($x_{pin}$, $y_{pin}$, $x_{ge}$, $y_{ge}$). In order to study the dynamics of this system, the equations of motion are described next for the rotational and translational along the Line of Action (LoA) using Eqs. (30) and (31), respectively.

$$m_i \ddot{y}_i + k_{si} y_i - c_m(r_2 \dot{\theta}_2 - r_1 \dot{\theta}_1 - \dot{x}_2 + \dot{x}_1 + \dot{e}_t) - k_m r_i(r_2 \theta_2 - r_1 \theta_1 - x_2 + x_1 + e_t) = 0, \tag{30}$$

$$j_i \ddot{\theta} + c_m r_i(r_2 \dot{\theta}_2 - r_1 \dot{\theta}_1 - \dot{x}_2 + \dot{x}_1 + \dot{e}_t) + k_m r_i(r_2 \theta_2 - r_1 \theta_1 - x_2 + x_1 + e_t) = T_i, \tag{31}$$

where $i = 1, 2$ (1 for gear, 2 for pinion).

These equations are solved iteratively using Matlab®/Simulink®.

## 5. The new gear-bearing simulation model

There are 34 DOF in the new model as opposed to the 16 DOF in the previous model [1]. This is illustrated in the schematic diagram of Fig. 8. The extra 18 DOF are due to the inclusion of the five-DOF bearing model (Fig. 3), and to the fact that translational DOF are now considered both along the Line of Action (LOA) and perpendicular to it (Figs. 3 and 7).

The main assumptions, on which the new model is based, are as follows.

(1) Shaft mass and inertia are lumped at the bearings or at the gears.
(2) Translational DOF are considered along the LoA and perpendicular to it, with the LoA aligned vertically.
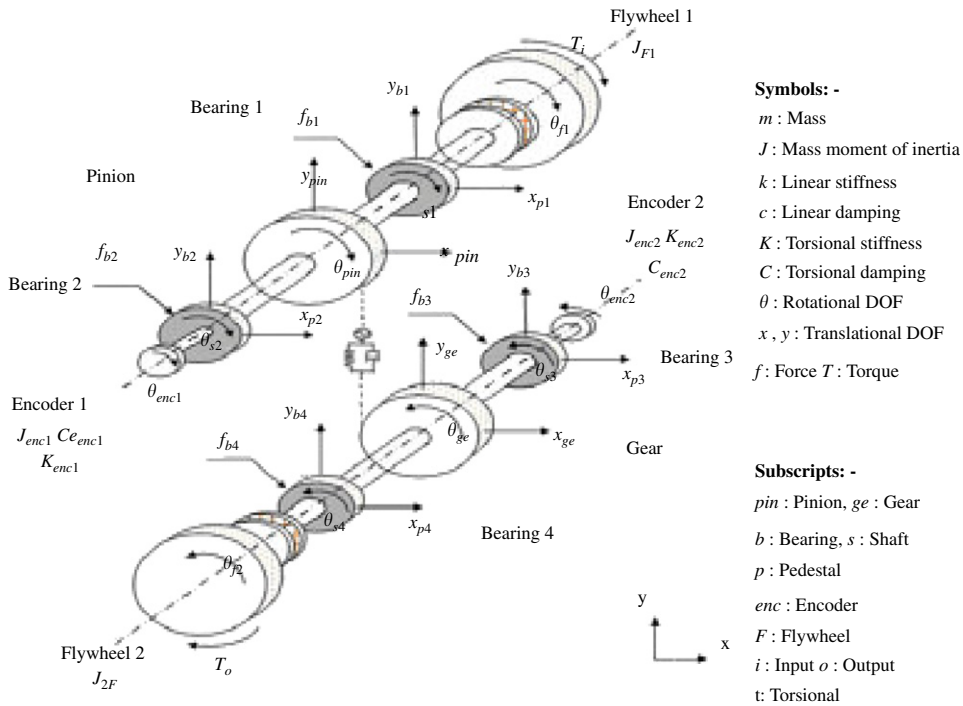(3) Two resonances of the gear casing are considered.

Fig. 8. Thirty-four-DOF dynamic model of the gear test rig (vertical direction *y* aligned with the Line of Action of the gears).

(4) The static TE of the gears (geometric and elastic) is included.
(5) Friction between the gear teeth is neglected.
(6) The gearmesh is assumed free from contact loss.
(7) The bearing stiffness is non-linear and time varying.
(8) Rolling element inertia is ignored.
(9) All rolling elements may have small random motions around their nominal positions and the average position determines the actual cage movement.
(10) There are no contact surface imperfections apart from the inner and outer race localised and extended defects, as well as localised rolling element defects, which are the subject of this study.
(11) Linear damping is applicable.

The values of the different parameters of the mathematical model can be obtained using Table 1. These have been calculated in terms of the geometric dimensions of the mechanical elements and were presented in Gao and Randall (2000) [7]. The damping ratios of the meshing gears and the flexible encoder rotor couplings were chosen as 5% and 35%, respectively (Gao and Randall, 2000) [7].

Table 2 lists the physical parameters for the bearing-pedestal system along with the extra DOF. The stiffness of the pedestal was selected to correspond to the 174-Hz frequency (lowest natural frequency of the casing in the vertical direction [1]). The stiffness of the sprung mass is selected so that a typical high frequency resonant response of the bearing is excited (15 kHz). The damping of the rolling elements was selected as 5%, the damping of the pedestal as 8%, while that for the sprung mass system was set to 5%.

The equations of motion describing this system can be written for the translational and rotational DOF using the general format equations given by Eqs. (32)–(34), respectively.

$$M\ddot{x} + c\dot{x} + kx = F_x, \tag{32}$$

$$M\ddot{y} + c\dot{y} + ky = F_y, \tag{33}$$

$$J\ddot{\theta} + C\dot{\theta} + K\theta = T. \tag{34}$$

Table 1
Mass, stiffness and damping of the flywheels, encoders, shafts, pinion and gear

|  | Mass | | Stiffness | | Damping | |
|---|---|---|---|---|---|---|
| Flywheel 1 | $J_{F1}$ (kg m$^2$) | 0.3647 | $K_{F1}$ (N m/rad) | 740 | $C_{F1}$ (N s/rad) | 10.20 |
| Flywheel 2 | $J_{F2}$ (kg m$^2$) | 0.5881 | $K_{F1}$ (N m/rad) | 740 | $C_{F2}$ (N s/rad) | 12.96 |
| Shafts | $J_{S1}$ (kg m$^2$) | $9.998 \times 10^{-4}$ | $K_{tS1}$ (N m/rad) | $4.241 \times 10^4$ | | |
|  | $J_{S2}$ (kg m$^2$) | $8.054 \times 10^{-5}$ | $K_{tS2}$ (N m/rad) | $4.241 \times 10^4$ | | |
|  | $J_{S3}$ (kg m$^2$) | $8.054 \times 10^{-5}$ | $K_{tS3}$ (N m/rad) | $4.241 \times 10^4$ | | |
|  | $J_{S4}$ (kg m$^2$) | $9.998 \times 10^{-4}$ | $K_{tS4}$ (N m/rad) | $4.241 \times 10^4$ | | |
| Pinion | $J_{pin}$ (kg m$^2$) | $1.766 \times 10^{-3}$ | | | | |
|  | $m_{pin}$ (kg) | 2.1208 | $k_S = k_{Sge} = k_{Spin}$ (N/m) | $7.42 \times 10^7$ | $c_m$ (N s/m) | 2594 |
|  | $J_{ge}$ (kg m$^2$) | $1.766 \times 10^{-3}$ | $k_m$ (mean) (N/m) | $3.718 \times 10^8$ | | |
| Gear | $m_{ge}$ (kg) | 2.1208 | | | | |
| Encoder1 | $J_{ec1}$ (kg m$^2$) | $2.525 \times 10^{-5}$ | $K_{ec1}$ (N m/rad) | 300 | $C_{ec2}$ (N s/rad) | 0.001 |
| Encoder2 | $J_{ec2}$ (kg m$^2$) | $2.525 \times 10^{-5}$ | $K_{ec2}$ (N m/rad) | 300 | $C_{ec2}$ (N s/rad) | 0.001 |

Table 2
Mass, stiffness and damping of the bearings

|  | Mass (kg) | | Stiffness | | Damping | |
|---|---|---|---|---|---|---|
| Bearings | $m_{S1}$ | 1.2638 | $K_{b1}$ (N/m$^{1.5}$) | $1.8978 \times 10^{10}$ | $c_{S1x} = c_{S1y}$ (Ns/m) | 1376.8 |
|  | $m_{S2}$ | 0.5134 | $K_{b2}$ (N/m$^{1.5}$) | $1.8978 \times 10^{10}$ | $c_{S2x} = c_{S21y}$ (Ns/m) | 877.6 |
|  | $m_{S3}$ | 0.5134 | $K_{b3}$ (N/m$^{1.5}$) | $1.8978 \times 10^{10}$ | $c_{S3x} = c_{S3y}$ (Ns/m) | 877.6 |
|  | $m_{S4}$ | 1.2638 | $K_{b4}$ (N/m$^{1.5}$) | $1.8978 \times 10^{10}$ | $c_{S4x} = c_{S4y}$ (Ns/m) | 1376.8 |
| Pedestal | $m_{p1}$ | 12.638 | $k_{p1x} = k_{p1y}$ (N/m) | $15.1056 \times 10^6$ | $c_{p1x} = c_{p1y}$ (Ns/m) | 2210.7 |
|  | $m_{p2}$ | 10.268 | $k_{p2x} = k_{p2y}$ (N/m) | $12.2728 \times 10^6$ | $c_{p2x} = c_{p2y}$ (Ns/m) | 1796.1 |
|  | $m_{p3}$ | 10.268 | $k_{p3x} = k_{p3y}$ (N/m) | $12.2728 \times 10^6$ | $c_{p3x} = c_{p3y}$ (Ns/m) | 1796.1 |
|  | $M_{p4}$ | 12.638 | $k_{p4x} = k_{p4y}$ (N/m) | $15.1056 \times 10^6$ | $c_{p4x} = c_{p4y}$ (Ns/m) | 2210.7 |
| Sprung system | $m_{r1}$ | 1 | $k_{r1}$ (N/m) | $8.8826 \times 10^9$ | $c_{r1}$ (Ns/m) | 9424.8 |
|  | $m_{r2}$ | 1 | $k_{r2}$ (N/m) | $8.8826 \times 10^9$ | $c_{r2}$ (Ns/m) | 9424.8 |
|  | $m_{r3}$ | 1 | $k_{r3}$ (N/m) | $8.8826 \times 10^9$ | $c_{r3}$ (Ns/m) | 9424.8 |
|  | $M_{r4}$ | 1 | $k_{r4}$ (N/m) | $8.8826 \times 10^9$ | $c_{r4}$ (Ns/m) | 9424.8 |

The different DOF in the new model are as follows. Ten rotational, similar to those in the 16-DOF model (two flywheels ($\theta_{f1}$, $\theta_{f2}$), one pinion and one gear ($\theta_{pin}$, $\theta_{ge}$), two encoders ($\theta_{enc1}$, $\theta_{enc2}$), four shafts ($\theta_{s1}$, $\theta_{s2}$, $\theta_{s3}$, $\theta_{s4}$)). The other 24 degrees are the translational ones, which are parallel to the Line of Action (pressure line) and perpendicular to it ($x$, $y$) directions. These are as follows: two for the pinion ($x_{pin}$, $y_{pin}$), two for the gear ($x_{ge}$, $y_{ge}$), 20 for the four bearings/casing ($x_{si}$, $y_{si}$, $x_{pi}$, $y_{pi}$, $y_{bi}$, $i = 1, 2, 3, 4$).

Matlab® matrix capability, and Simulink® simulation environment were employed to solve the set of the equations of motion using the ordinary differential equation solver (ode45), which is based on Runge–Kutta method. The bearing model was implemented as an S-function (special function for Simulink®), which was dynamically updated as the simulation proceeded. The load-dependant non-linearity of gearmesh stiffness was implemented as a "look-up table" with cubic spline interpolation.

## 6. Experimental and simulated results

Different kinds of faults were introduced to a number of bearings, in a previous study by Ho [25], to investigate the use of Self Adaptive Noise Cancellation (SANC) for bearings in a gearbox environment. These have been used here to investigate the effectiveness of the simulation model.
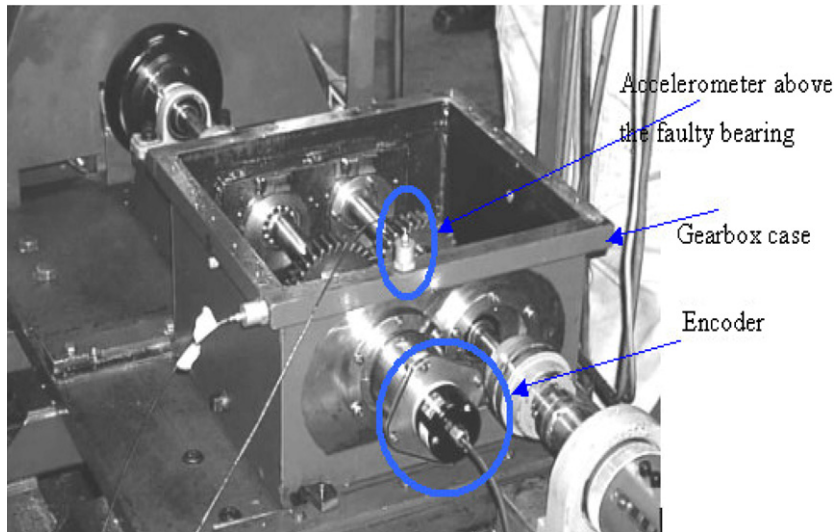
Fig. 9. The spur gear rig.



Fig. 10. Bearing under the test (Koyo 1205).

In order to compare the simulation results to those obtained experimentally, the different types of faults were tested under a 50-N m load, while setting the output shaft speed to 10 Hz (600 rpm). Vibration signals were collected using an accelerometer positioned on the top of the gearbox casing above the defective bearing. The 1.35-s (65,536 samples) signals were sampled at 48 kHz. A photo-reflective switch was placed near the output shaft to measure its speed by providing a once per rev tacho signal. The torque for each case was measured at the input shaft.

A photograph of the rig showing the position of the accelerometer and the encoder at the output shaft is shown in Fig. 9.

The bearings under test (Fig. 10) are double row self-aligning (Koyo 1205) with an angle of contact of $0°$, a ball diameter of 7.12 mm and a pitch diameter of 38.5 mm.

The defect frequencies (frequencies at which the ball passes the defect on the outer race (BPFO) or the inner race (BPFI)) can be estimated for the outer race as 48.9 Hz and for the inner race as 71.1 Hz. The fundamental train frequency (FTF) is estimated at 4.1 Hz, while the speed at which the balls spin (BSF) is 26.5 Hz.

### 6.1. Outer race localised faults

A notch fault was introduced into the outer race of the double-row ball bearing. This was performed using electric spark erosion and generated a gap in the outer race with a rectangular cross-section (Fig. 11). The bearings were positioned such that the outer race faults were always in the loaded zone as this is where a fault would most likely occur [25].

The notch fault dimensions were inserted into the bearing's S-function to simulate the vibration generated from the test rig as a result of this fault. In order to take into account the differences originating from aligning the Line of Action (LoA) of the gear with the vertical direction in the simulation model (pressure angle in the actual case is $20°$ from the vertical) the position of the spall was shifted by $20°$ from the centre of the load zone. The width of the fault was set to 0.8 mm, while that of the depth was set to 19.1 μm in the simulated case, as this would be the maximum depth that the ball would be able to touch. Additive pink noise is added to the obtained signals so that a reasonable SNR is achieved (15–25 dB).

#### 6.1.1. Time domain acceleration signals

The time domain signals (acceleration ($m/s^2$)), representing one complete revolution of the gear/pinion set (4800 samples representing 32 gearmesh teeth), for both a simulated and an actual (experimental) localised outer race fault are shown in Fig. 12.

Fig. 12 shows the dominant effect of the gear signal. Albeit, the bearing fault signature is there, it is very hard to distinguish it in both the measured and the simulated signals. The signals are highly dominated by the gear components and of no impulsive nature (the time kurtosis for the simulated signal is −0.9682, while that of the measured signal is −0.1066). Note the good resemblance between the two signals in terms of the pattern and the scale.

To gain more insight into the signals, the first five tooth meshes are expanded and plotted in Fig. 13. The defect signature can now be seen clearly around the sample number 500 (circled) as a disruption of the high frequency component of the signal (see Section 4 for explanations of the source of the high frequency component). This happens as a result of a ball passage over the spall region as earlier described in Section 3.5. The high frequency component seen throughout the signal represents both the multiplicative noise effect (as a result of adding noise to the transmission) and the bearing contribution (a direct result from the randomness introduced to the ball positions).

To investigate the contributions of both the gear and the bearing signals, the power spectra for both the good and the faulty bearings are discussed next for the simulated and experimental cases.

#### 6.1.2. Comparison of the power spectra

Power spectral densities were calculated using Welch's averaged, modified periodogram method (psd function in Matlab®). A hanning window of Nfft = 512 samples was used to estimate the power spectrum of
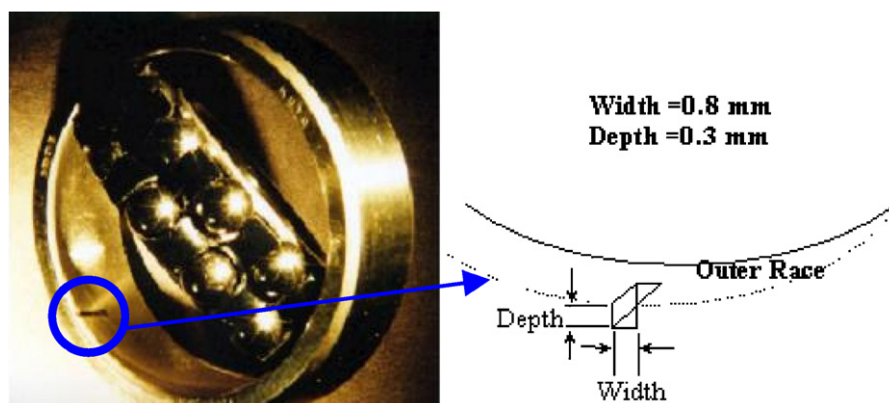


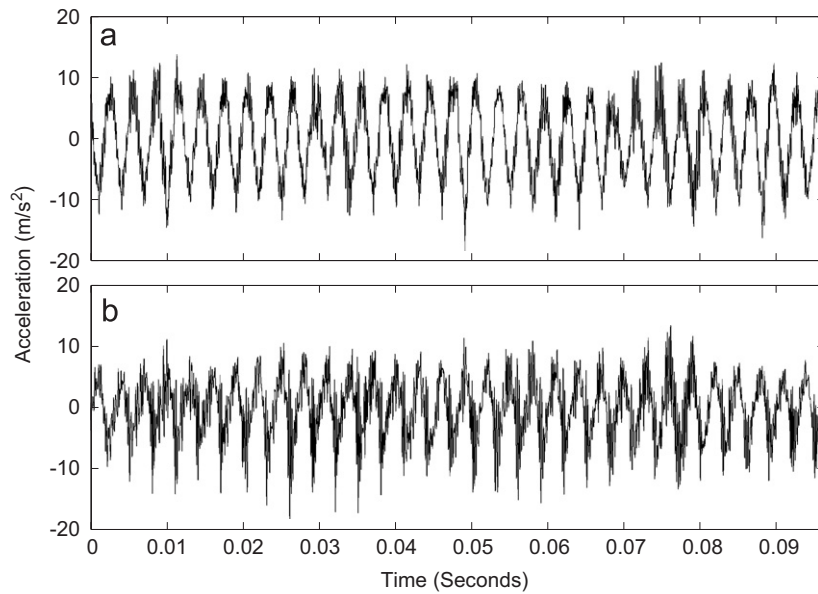Fig. 11. Outer race fault insertion and dimensions [14].

Fig. 12. (a) Simulated accelerometer signal with localised outer race fault, (b) actual measured accelerometer signal (experimental) for the localised outer race fault.
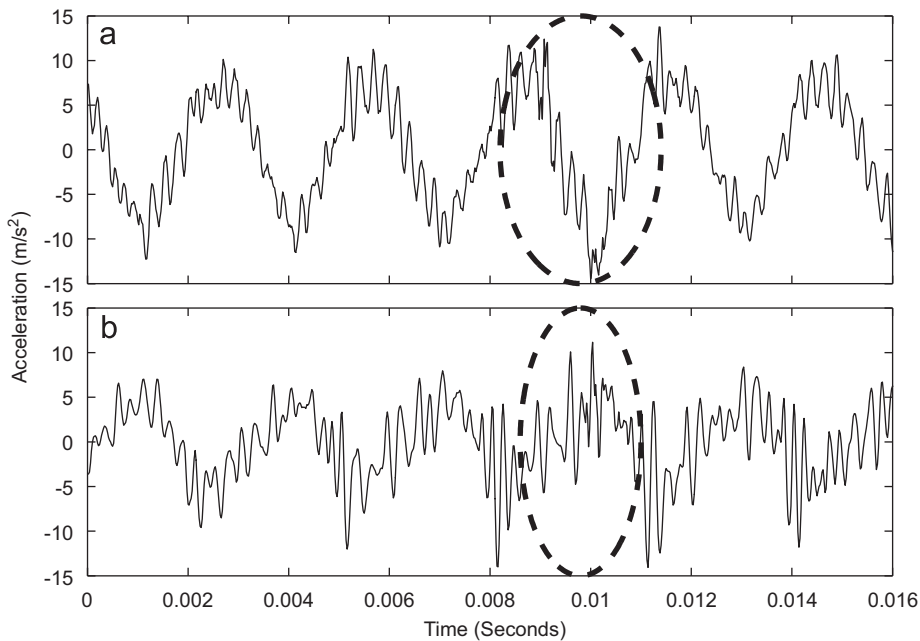


Fig. 13. Five-gearmesh teeth: (a) simulated (b) measured. Circled: outer race defect signature.

each signal. The power spectrum density (resolution of 93.5 Hz/line) is not used as an analysis technique in this instance, but only as a comparison technique between the faulty and good cases and so did not need to be calculated using a high resolution (larger Nfft). It has been explained in many papers that the additive components at the low harmonics of the ballpass frequency have negligible amplitude in acceleration signals (e.g. Ref. [25]), and this is the reason for using envelope analysis.
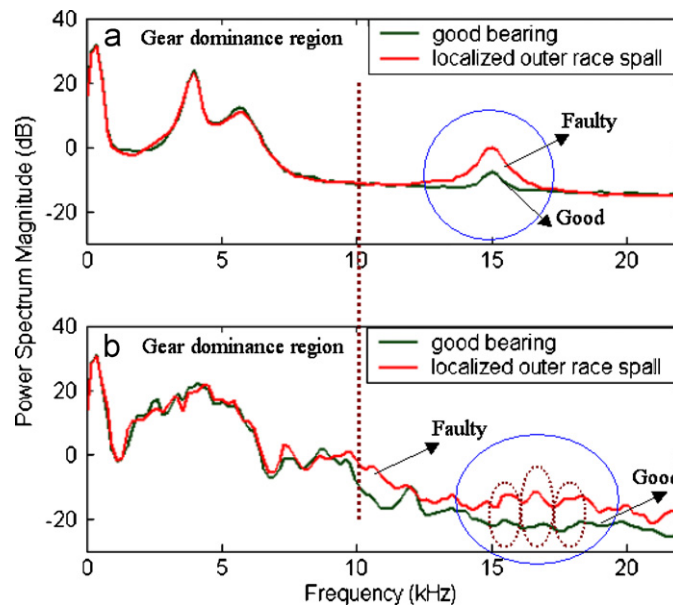
Fig. 14. Power spectrum comparison for good and outer race defect bearings: (a) simulated, (b) experimental.

Spectrum comparisons for the good and the faulty outer race bearings are shown in Fig. 14. Both experimental and simulated results exhibit the same behaviour, which shows an increase in the level of the power spectra in the high frequency range (maximum bands circled) as a result of the defect in the outer race.

It is noticed that the response due to the introduction of the defect is concentrated at around the 15 kHz in the simulated signal, while it excites several resonances in the measured one. The lower frequency range (up to 10 kHz) is dominated by the gearmesh, and shows no change for the good and faulty cases. Note that in the simulation model, only two resonances have been considered when modelling the gearbox casing (only one at low frequency) but most interestingly, the behaviour and the excitation pattern are quite similar in both measured and simulated signals. The other low frequency resonances in the simulated signal are associated with the internal components.

### 6.1.3. Spectral Kurtosis (SK) analysis and the envelope spectra

SK [26] is quite powerful for determining the frequency bands dominated by the bearing fault signals, which contain resonance frequencies excited by the faults. This information is required in order to choose the optimum frequency band to perform the "envelope analysis" on the bearing signals. Traditionally, the optimum band selection is recommended based on the results of a spectrum comparison with previous data (fault-free data), on the basis that if the change were due to a bearing fault, the band with the greatest dB change would automatically represent that with the largest SNR of bearing signal to background noise [27].

Figs. 15 and 16 show the results of processing the simulated and measured signals, respectively, using the SK. Fig. 15 indicates that the optimum filter to extract the impulses in the system (the one with the highest kurtosis) is the one with a centre frequency of 13.557 kHz and with a bandwidth of 1600 Hz. For the measured signal, the optimum filter is the one with a centre frequency of 15.274 kHz and of a bandwidth of 1900 Hz.

The filtered time domain signals and the squared envelope spectra for the simulated data (demodulated from 12.757 to 14.357 kHz) and the experimentally measured data (demodulated from 14.324 to 16.224 kHz) are shown in Figs. 17 and 18, respectively.

Note the substantial similarities in the filtered signals and in the envelope spectra, and how the BPFO ($\approx 49$ Hz) and its harmonics are very clear, thus denoting the existence of an outer race fault.
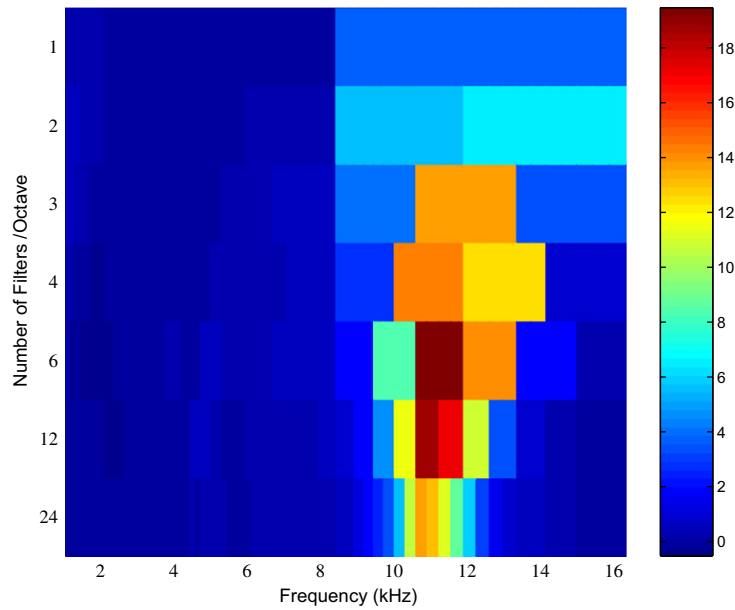
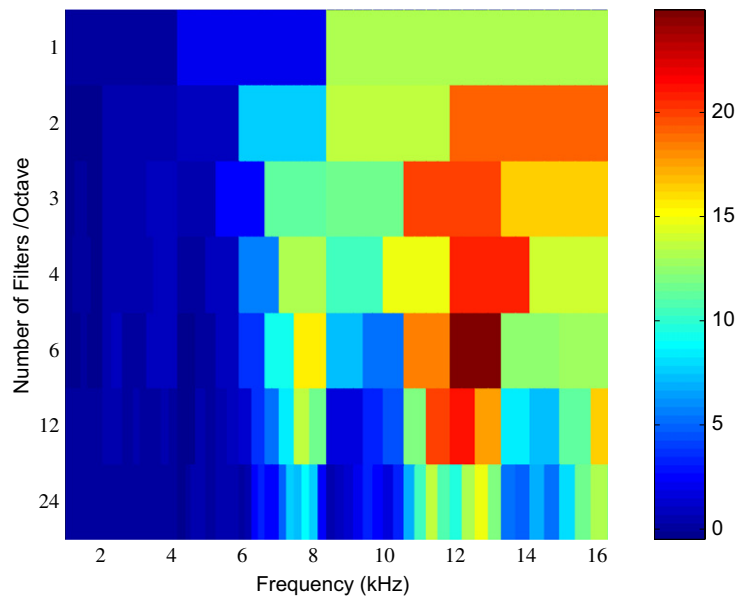Fig. 15. SK analysis for the simulated signal.



Fig. 16. SK analysis for the measured signal.

### 6.1.4. Double impulse phenomenon

Interesting results were obtained when inspecting the signature of the bearing as obtained by the filtered signals, in that the transient was found to be composed of two parts. This was found to agree well with actual measurements when carefully examined as illustrated in Fig. 19 and has a theoretical background that supports the findings [28,29]. The spacing between the two impulses is 1.3 ms, which corresponds to the 0.8 mm width of the fault.
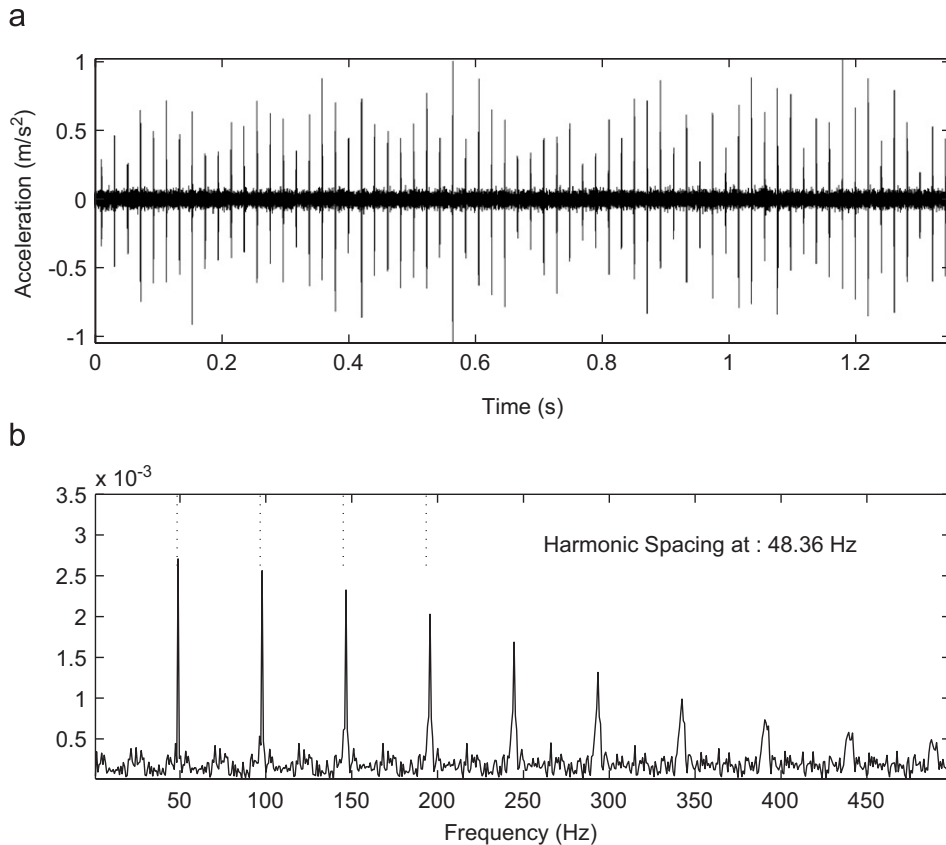
Fig. 17. Simulated signal for a localised outer race fault: (a) filtered signal, (b) squared envelope spectrum.

Epps and McCallion [28] indicated that there might be two parts to the defect signal—the first part originating from the entry of the rolling element into the fault and the second part due to the departure of the rolling element from the fault. Epps and McCallion also mentioned that as the size of the fault increases the separation between the two points, that is the time to impact, increases and if each impulse response can be seen in the time series, the size of the fault can be diagnosed.

Fig. 20 [29] illustrates a recoded waveform from a helicopter gearbox bearing. The outer race has a spall that takes approximately 0.3 ms for the rolling element to traverse. About six cycles into the transient, there is a slight gap, due to a phase reversal. The transient begins when the ball enters the fault and energy is released. About 0.3 ms later, the ball exits the fault and recompresses. This second impact creates a new wave which interferes with the first, resulting in a phase shift (the gap) [29].

The clarity of impulses can be enhanced by using the MED technique [30].

### 6.2. Localised inner race faults

An inner race localised fault was also introduced into the bearing in a similar way to the outer race fault. The fault spanned over half of the race width so that only one set of balls was impacting with the fault. The width of the fault was set to 0.8 mm (actual physical dimension), while the depth was set to 27.6 µm, as this would be the maximum depth that the ball would be able to touch (physical depth of the fault is 0.3 mm). A preload interference of $-3$ µm was used in this case.

#### 6.2.1. Time domain acceleration signals

Fig. 21 shows the time domain acceleration signals (one revolution) for measured and simulated signals in the case of the localised inner race fault. The similarity between the two signals in terms of the impact pattern is quite obvious. Note how the largest impact occurs when the inner race goes through the load zone.
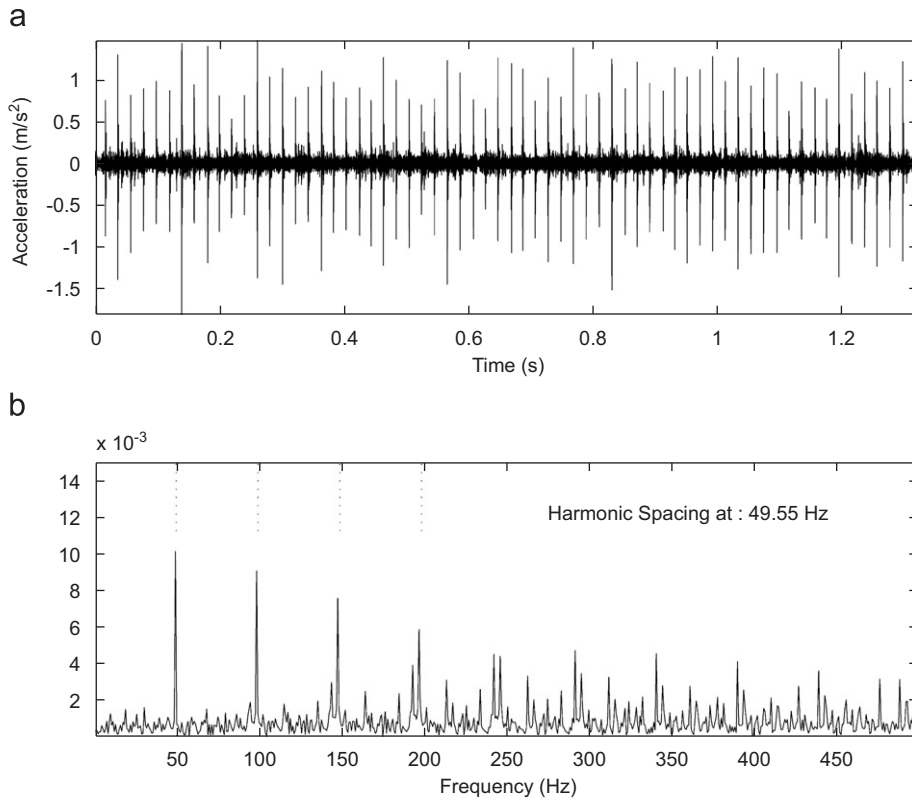
Fig. 18. Measured signal for a localised outer race fault: (a) filtered signal, (b) squared envelope spectrum.

The impacts seen outside the load zone are due to the preloading of the bearings. This has been presented in the bearing model by setting the clearance value ($c$)—Eq. (13)—to an arbitrary value of $-3\,\mu m$.

### 6.2.2. Comparison of the power spectra

The raw spectrum comparison for both the experimental and simulated cases is presented in Fig. 22, which shows a very good agreement of the major features (keeping in mind that the model has only two resonances representing the casing).

It is noted that the response due to the introduction of the localised defect is concentrated around the high frequency damped resonance in the simulation (15 kHz), and noticeably extends beyond the 15 kHz. In the measured signal, the excitation covers the whole region above the 10 kHz, while no effect is clear at the lower region (dominated by the gears). Note how the effect of the localised fault in both the inner and outer race gave the same effect on the spectrum, which makes it hard to distinguish the source of the fault from only comparing the good and the faulty spectra.

### 6.2.3. Comparison of the filtered signals and the envelope spectra

In order to extract the impulses from the raw signals, both measured and simulated data were subjected to the same processing techniques, namely AR filtration (pre-whitening) [31], SK and the Envelope analysis. The results are shown in Figs. 23–26, respectively.

The SK analysis for the simulated and the measured signals are presented in Figs. 23 and 24, respectively. Note the subsequent similarities in the SK analysis in both simulated and measured cases (even in terms of the values). The optimum filter for the simulated signal (the circled one) has a centre frequency of 13.607 kHz and a bandwidth of 3400 Hz. For the measured signal, the optimum filter is the one with a centre frequency of 10.800 kHz and a bandwidth of 2025 Hz.
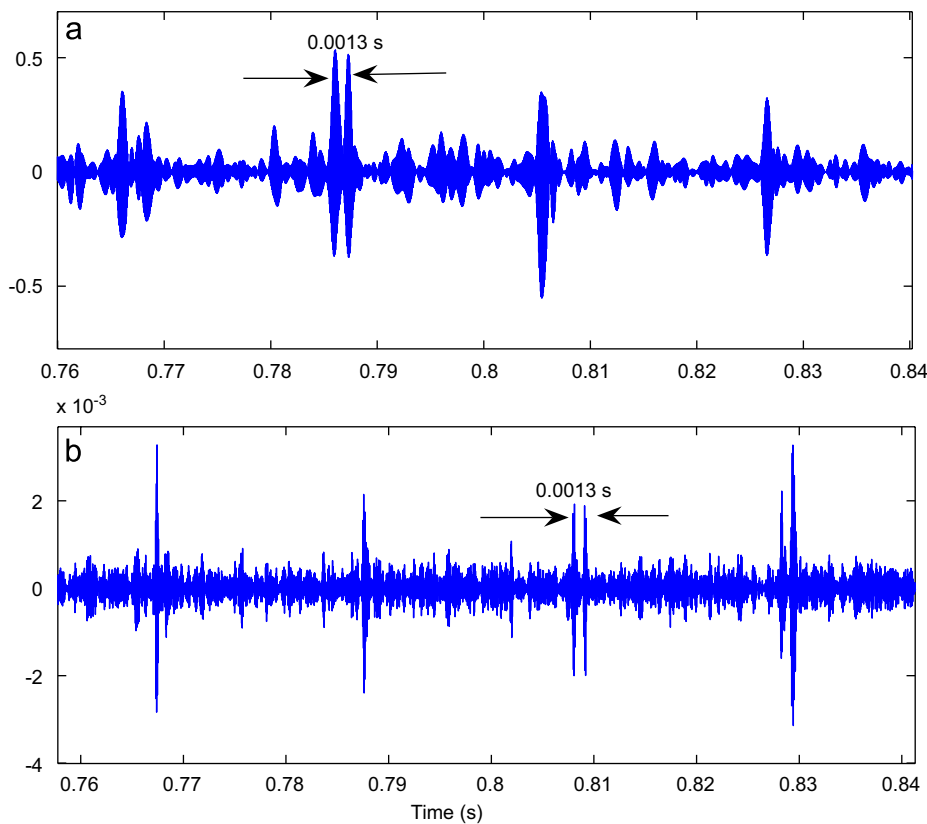
Fig. 19. Bandpassed filtered signals (one complete rotation of the shaft) with a spall in the outer race: (a) measured, (b) simulated.
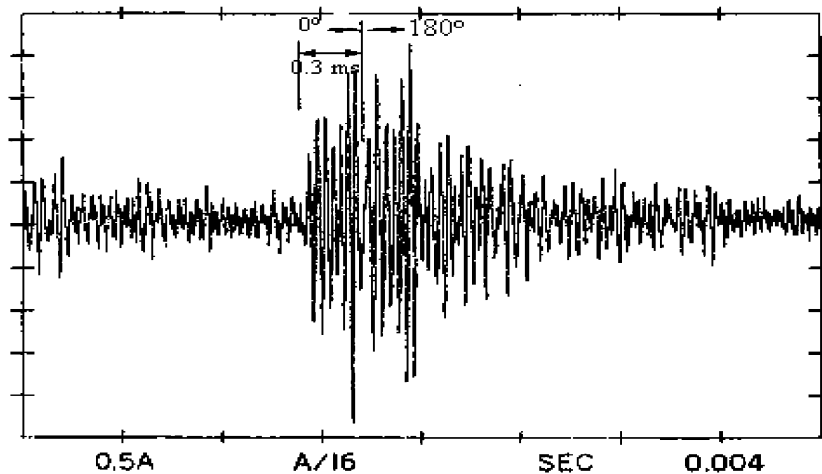


Fig. 20. Bandpassed filtered trace from helicopter gearbox bearing with a spall in the outer race [18].

Figs. 25 and 26 show the filtered signal obtained via the SK optimum filter and the corresponding squared envelope spectrum for both the simulated and the measured signals, respectively. The similarities in the filtered signals and in the envelope spectra are obvious, which in both cases clearly indicate an inner race fault (BPFI 71.1 Hz harmonics modulated by shaft rotational speed 10 Hz). However, the modulation of the simulated signal is somewhat stronger (agreeing with the time domain signals). A possible explanation of this could be
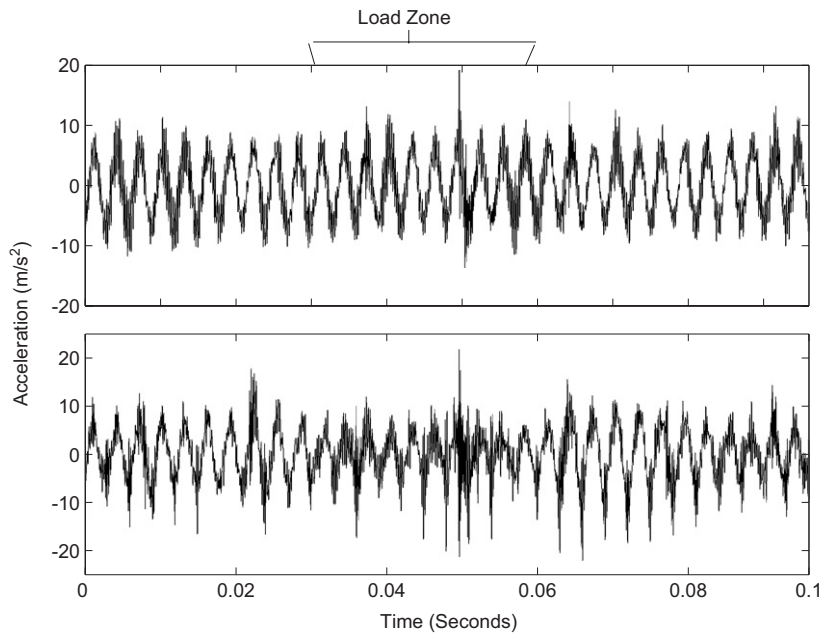
Fig. 21. Time domain signals for localised inner race fault (one revolution): (a) simulated, (b) measured.
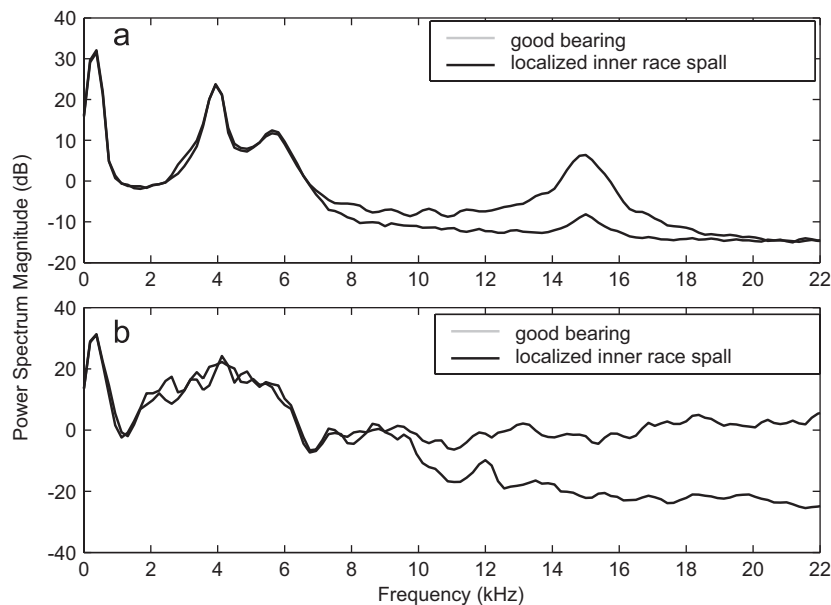


Fig. 22. Power spectra comparison for the good and inner race defective bearings: (a) simulated, (b) experimental.

a small amount of unbalance; meaning that the load is not completely uni-directional, which could be easily simulated.

The impulsive nature is examined by zooming in at three impulses (24.c: simulated, 25.c: measured), and by a further focus on one impulse (24.d and 25.d). Note the general similarities between the simulated and measured cases; however, the damping of the two impulses is different and the double impulse phenomenon is clearer in the simulated signal.
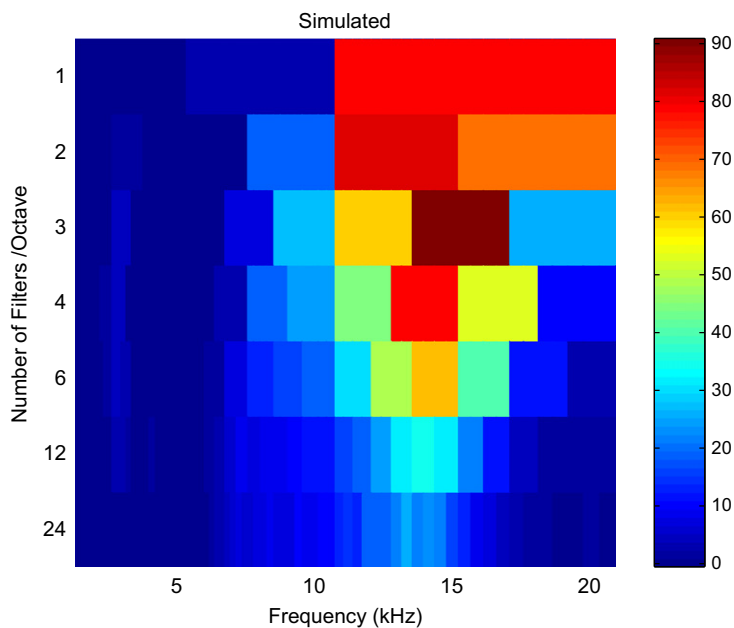
Fig. 23. SK analysis for the simulated signal with a localised inner race fault.
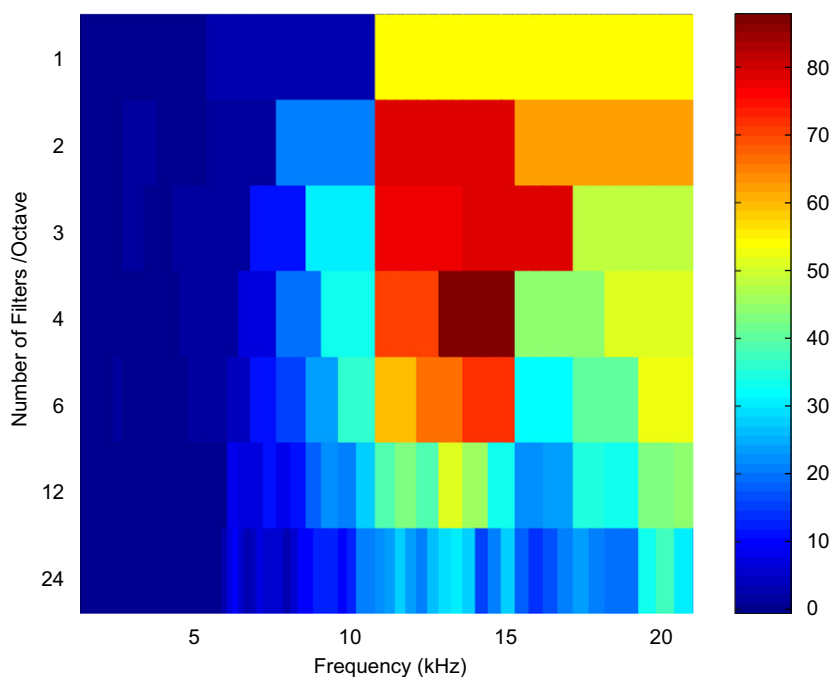


Fig. 24. SK analysis for the measured signal with a localised inner race fault.

## 6.3. Rolling element localised faults

A notch fault was introduced into one of the rolling elements (balls) in a similar way to those introduced earlier to both inner and outer races using electric spark erosion. The electrode was designed in such a way that the fault would extend over an included angle of 60° over the ball's surface. The generated gap in the ball has a rectangular cross-section (0.5 mm in depth and 0.5 mm wide).
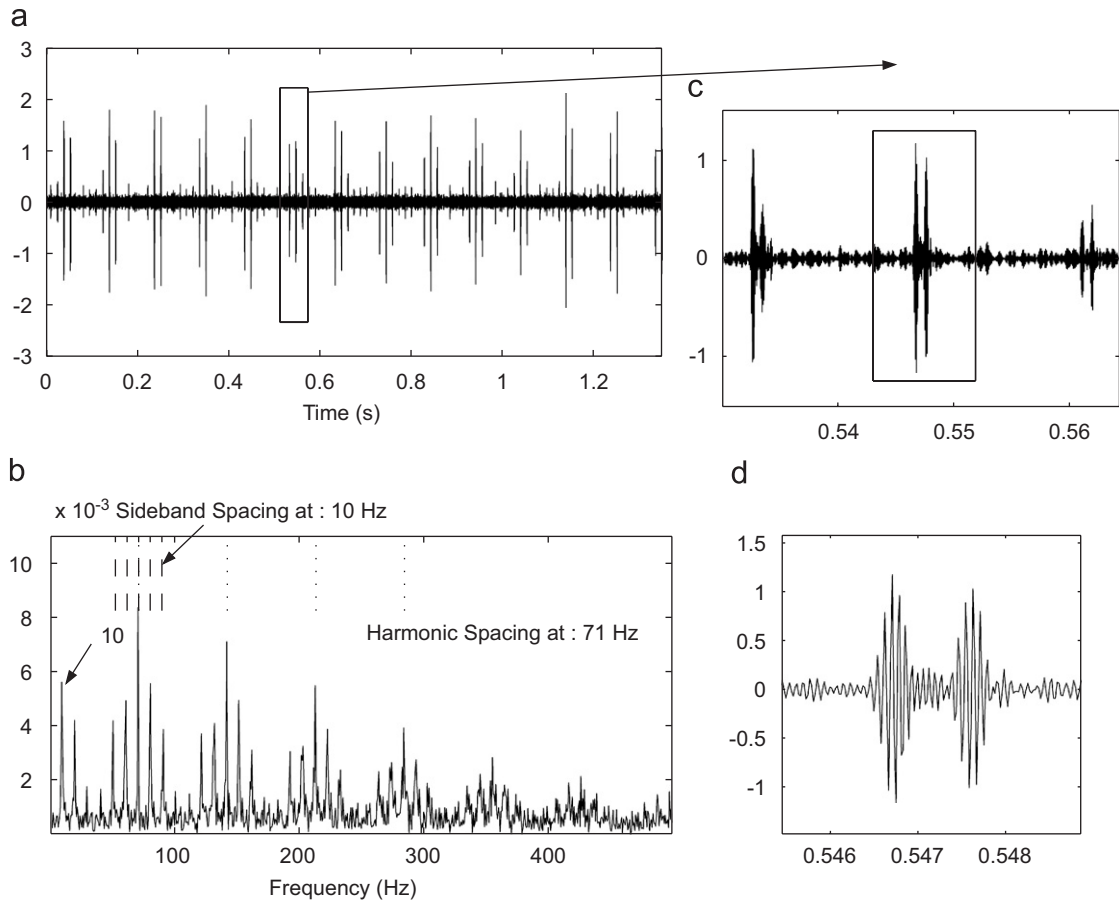
Fig. 25. Simulated results: (a) filtered signal, (b) squared envelope spectrum, (c) zoom in on three impulses, (d) clear double impulse.

In the bearing simulation function, the width of the fault was set to 0.5 mm, while the depth was set to 10.7 μm when the ball touches the inner race and 7.4 μm when it touches the outer race (because of the respective convexity/concavity of the races). A preload value of −3 μm was used.

### 6.3.1. Time domain and the power spectra comparison

Fig. 27 shows the accelerometer time domain signals for one complete rotation of the gears for both the simulated and measured signals. The effect of the fault is very clear at the centre of the load zone. The pattern of the impacts in both simulation and measured signals is the same, except that in the simulation signal the impulses are more obvious and less damped. Note that the differences are much smaller in bandpass-filtered signals given as follows.

To see the effect of the rolling element fault on the power spectra, both faulty simulated and the measured signals are compared with their fault-free counterparts and the result is plotted in Fig. 28. The rolling element localised fault is no exception to what has been earlier discussed for the localised faults in the inner and outer races. In both, the simulation and the experimental cases, the localised ball defect excites the frequency region above 10 kHz. In the simulation, this is centred around 15 kHz, while in the measured signal; it excites a wide range of the structure resonances.

### 6.3.2. Envelope analysis

The signature of the rolling element faults is inspected through the filtered signals (obtained via the SK filter) and their corresponding squared envelope spectra. These are plotted in Figs. 29 and 30 for the simulated
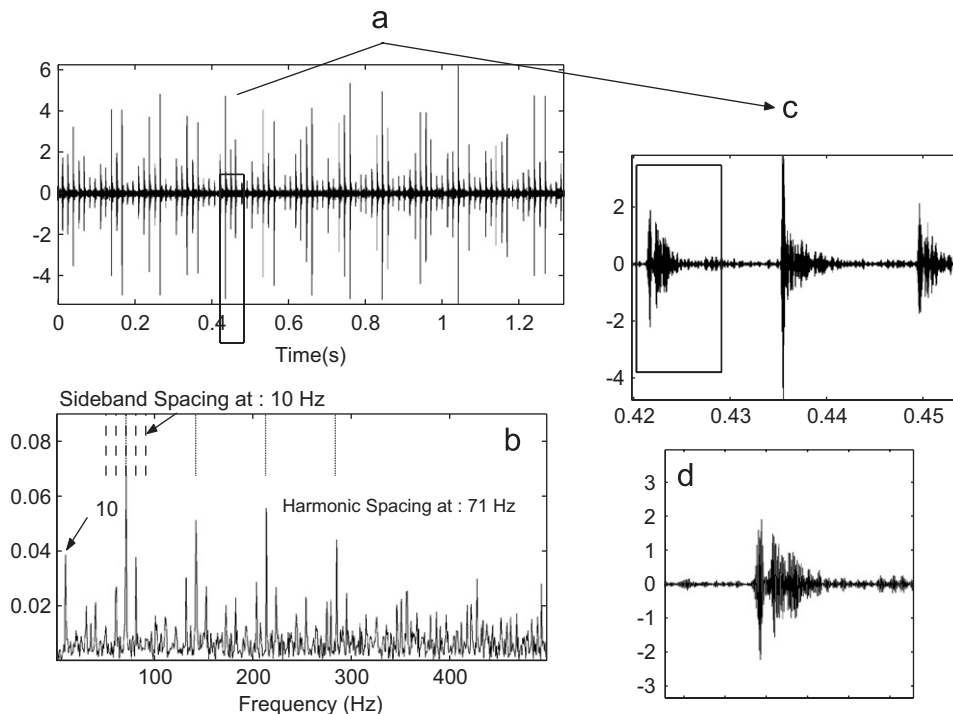
Fig. 26. Experimental results: (a) filtered signal, (b) squared envelope spectrum, (c) zoom in on three impulses, (d) clear double impulse.
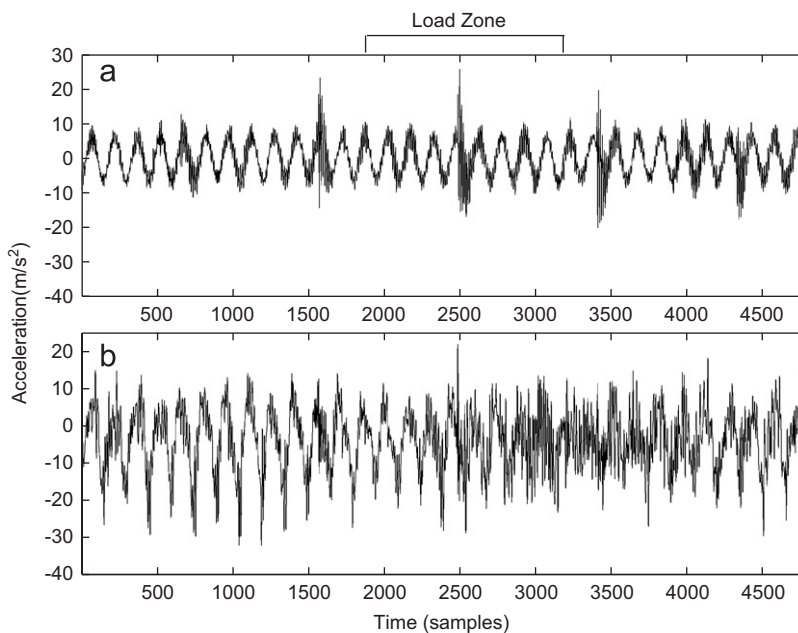


Fig. 27. Time domain signals for localised rolling element fault: (a) simulated, (b) measured.

and experimental cases, respectively, and show a much better agreement between the simulated and the actual signals than the unfiltered signals of Fig. 27. The dominant frequency is ($2 \times$ ball spin frequency (BSF)) (52 Hz) as the fault impacts twice during one complete rotation of the ball (on the inner and the outer races), which is modulated by the cage speed (4 Hz). Note also the existence of the BSF components in the squared
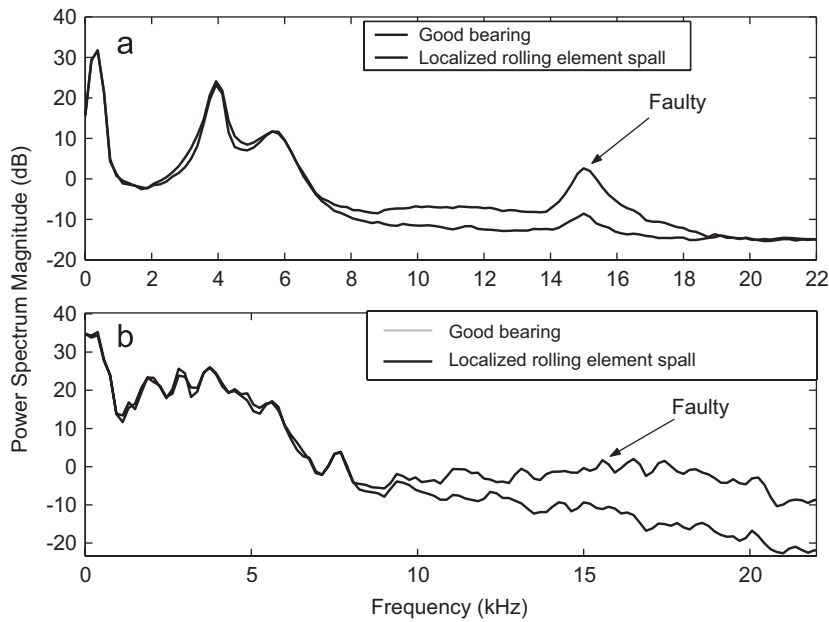
Fig. 28. Power spectra comparison for the good and inner race defective bearings: (a) simulated, (b) experimental.
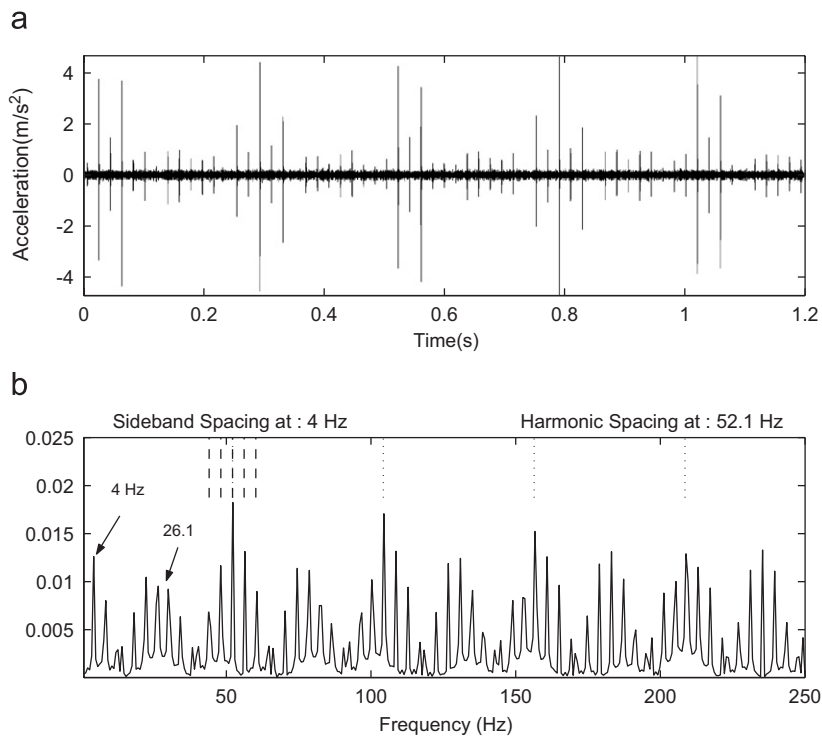


Fig. 29. Envelope analysis for the simulated localised rolling element fault: (a) filtered signals, (b) squared envelope spectra.

envelope spectra for both the simulated and the measured signals. This is because of the variation of the impact severity between the inner and outer races; due to the difference in race curvature. If the defect depths were modelled to be the same for both the races, only harmonics of $(2 \times \text{BSF})$ would appear in the squared envelope spectra.
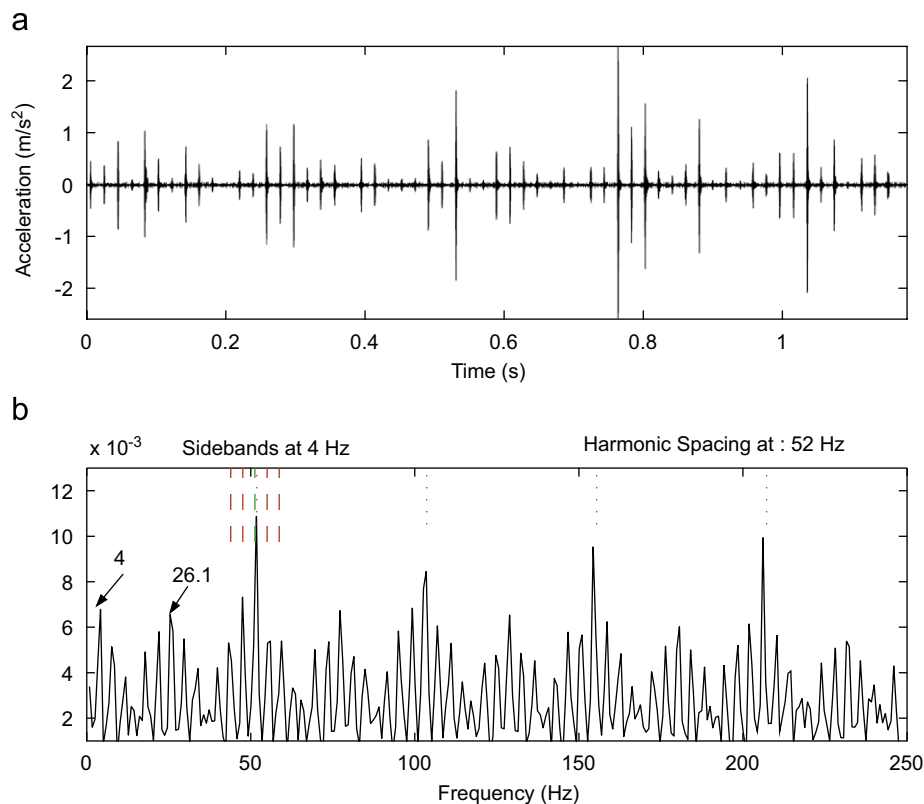
a



b



Fig. 30. Envelope analysis for the experimental localised rolling element fault: (a) filtered signals, (b) squared envelope spectra.

## 7. Conclusion

This paper presented a combined gear/bearing dynamic model for a gearbox test rig to study the interaction between gears and bearings in the presence of faults. The 34-DOF model of the test rig is a lumped mass parameter model which now has the capacity of modelling different fault types in the different parts of the bearing (inner race, outer race and the rolling elements). This is in addition to its original capacity for modelling spalls and cracks in the gears.

The new model takes into consideration the slippage in the bearings, the Hertzian contact and the non-linearity of the bearing stiffness (time variant). The way of modelling the spall region to reflect the actual path of the rolling element presents a new variation from the original model. The simulated signals of the localised defects were found to have the same basic characteristics as measured signals and, moreover, showed clearly a characteristic that is traced in the measured signals, and also referred to in the literature, of double pulses corresponding to entry into and exit from a localised fault. The similarity between simulated and measured signals subjected to a range of diagnostic techniques suggests that the model can be used efficiently to simulate faults of different size and locations.

The model is further extended to include the simulation of the extended faults (rough surface) and a full discussion on that can be found in the second part of this paper.

## Acknowledgement

# References

[1] H. Endo, A study of gear faults by simulation, and the development of differential diagnostic techniques, Ph.D. Dissertation, UNSW, Sydney, 2005.

[2] N.S. Feng, E.J. Hahn, R.B. Randall, Using transient analysis software to simulate vibration signals due to rolling element bearing defects, in: Proceedings of the 3rd Australian Congress on Applied Mechanics, Sydney, 2002, pp. 689–694.

[3] N. Sawalhi, R.B. Randall, H. Endo, Simulating gear and bearing interactions in the presence of faults, Paper presented at the 7th IFToMM-Conference on Rotor Dynamics, Vienna, Austria, 25–28 September, 2006.

[4] N. Sawalhi, R.B. Randall, Simulation of the vibrations produced by extended bearing faults in gearboxes, Paper presented at the First Australasian Acoustical Societies' Conference, Christchurch, New Zealand, November, 2006.

[5] P.J. Sweeney, Transmission error measurement and analysis, Ph.D. Dissertation, UNSW, Sydney, 1994.

[6] S. Du, Dynamic modelling and simulation of gear transmission error for gearbox vibration analysis, Ph.D. Dissertation, UNSW, Sydney, 1997.

[7] Y. Gao, R.B. Randall, Simulation of geometric, static and dynamic gear transmission errors, Report CEVA-2000-01, Centre of Expertise in Vibration Analysis, UNSW, Sydney, 2000.

[8] H. Endo, R.B. Randall, C. Gosselin, Differential diagnosis of spalls vs cracks in the gear tooth fillet region, Journal of Failure Analysis and Prevention 4 (5) (2004) 57–65.

[9] G. Lundberg, A. Palmgren, Dynamic capacity of rolling bearing, Acta Polytechnic Mechanical Engineering Series 1 (3) (1947).

[10] F.J. Harris, Rolling Bearing Analysis I, Wiley, New York, 1966, pp. 148.

[11] P.K. Gupta, Transient ball motion and skid in ball bearings. Transactions of the American Society of Mechanical Engineers, Journal of Lubrication technology (April) (1975) 261–269.

[12] I. Howard, A review of rolling element bearing vibration: detection, diagnosis and prognosis, DSTO-AMRL Report, DSTO-RR-00113, 1994, pp. 35–41.

[13] J. Sopanen, A. Mikkola, Dynamic model of a deep-groove ball bearing including localized and distributed defects. Part 1: Theory, in: Proceedings of the Institution of Mechanical Engineers, vol. 217, Part K: J. Multi-body Dynamics, 2003, pp. 201–211.

[14] M. Tiwari, K. Gupta, O. Prakash, Effect of radial internal clearance of a ball bearing on the dynamics of a balanced horizontal rotor, Journal of Sound and Vibration 238 (2000) 723–756.

[15] M. Tiwari, K. Gupta, O. Prakash, Dynamic response of an unbalanced rotor supported on ball bearings, Journal of Sound and Vibration 238 (2000) 757–779.

[16] Y.H. Wijnat, J.A. Wensing, G.C. Van Nijen, The influence of lubrication on the dynamic behaviour of ball bearings, Journal of Sound and Vibration 222 (4) (1999) 579–596.

[17] S. Fukata, E.H. Gad, T. Kondou, T. Ayabe, H. Tamura, On the vibration of ball bearings, Bulletin of JSME 28 (239) (1985) 899–904.

[18] J. Sopanen, A. Mikkola, Dynamic model of a deep-groove ball bearing including localized and distributed defects. Part 2: Implementation and results, in: Proceedings of the Institution of Mechanical Engineers, vol. 217 Part K: J. Multi-body Dynamics, 2003, pp. 213–223.

[19] P.K. Gupta, Advanced Dynamics of Rolling Element Bearings, Springer, London, 1984.

[20] T.C. Lim, R. Singh, Vibration transmission through rolling element bearings, Part I: Bearing stiffness formulation, Journal of Sound and Vibration 139 (2) (1990) 179–199.

[21] T.C. Lim, R. Singh, Vibration transmission through rolling element bearings, Part II: System studies, Journal of Sound and Vibration 139 (2) (1990) 201–225.

[22] A. Liew, N.S. Feng, E.J. Hahn, Transient rolling element bearing systems, Transactions of the ASME Turbines and Power 124 (4) (2002) 984–991.

[23] R.B. Randall, Frequency Analysis, third ed., Bruel & Kjaer, Denmark, 1987.

[24] I. Howard, S. Jia, J. Wang, The dynamic modelling of a spur gear in mesh including friction and a crack, Mechanical Systems and Signal Processing 15 (5) (2001) 831–853.

[25] D. Ho, Bearing diagnostics and self-adaptive noise cancellation, Ph.D. Dissertation, UNSW, Sydney, 1999.

[26] J. Antoni, The Spectral Kurtosis: a useful tool for characterising nonstationary signals, Mechanical Systems and Signal Processing 20 (2) (2006) 282–307.

[27] R.B. Randall, Computer aided vibration spectrum trend analysis for condition monitoring, Maintenance Management International 5 (1985) 161–167.

[28] I.K. Epps, H. McCallion, An investigation into the characteristics of vibration excited by discrete faults in rolling element bearings, in: Proceedings of the Annual Conference of the Vibration Association of New Zealand, Christchurch, 1994.

[29] M.J. Dowling, Application of non-stationary analysis to machinery monitoring, IEEE 0-7803-0946-4/93 (1993) I 59–I 62.

[30] N. Sawalhi, R.B. Randall, H. Endo, The enhancement of fault detection and diagnosis in rolling element bearings using minimum entropy deconvolution combined with spectral kurtosis, Mechanical Systems and Signal Processing 21 (6) (2007) 2616–2633.

[31] N. Sawalhi, R.B. Randall, Spectral Kurtosis enhancement using autoregressive models, in: Proceedings of the ACAM Conference, Melbourne, Australia, 2005.